Journal of Mining and Environment (JME) Vol. 17, No. 5, 2026, 1753-1780

Shahrood University of Technology

Journal of Mining and Environment (JME)

Journal homepage: www.jme.shahroodut.ac.ir

Iranian Society of Mining Engineering (IRSME)

Influence of Joint Conditions Relative to the Incident Bar Dynamic Ioading on the Fragment Size of Iron Ore

Shadman Mohammadi Bolbanabad[1], Masoud Monjezi[1], and Vahab Sarfarazi[2*]

1. Department of Mining Engineering, Faculty of Mining and Materials, University of Tarbiat Modares, Tehran, Iran
2. Department of Mining Engineering, Hamedan University of Technology, Hamedan, Iran

Article Info

Received 26 July 2025

Received in Revised form 16 August 2025

Accepted 10 October 2025

Published online 10 October 2025

DOI: 10.22044/jme.2025.16579.3241

Keywords

SHPB

Non-persistent edge notch

Fragment size distribution

Failure pattern

Dynamic compressive strength

Abstract

The characteristics of fragment size distribution caused by blasting operations in open-pit mines have a direct impact on the economic performance and productivity of mining companies. In this study, dynamic impact loading tests were carried out using the Split Hopkinson Pressure Bar (SHPB) system under a constant pressure of 12.5 MPa to investigate the influence of both the edge notch length and its position relative to the incident bar on the size distribution of fragmented iron ore. By analyzing the fragmentation distribution characteristics of specimens subjected to controlled laboratory impact loading, this study focuses on fundamental rock breakage mechanisms relevant to blasting operations in open-pit iron ore mines, where the fragmented material classified into three particle size categories: large, medium, and fine fragments. Based on this classification, the variation in the mass percentage of fragments with respect to notch length and its position relative to the incident bar was investigated. Ultimately, within the context of laboratory-scale fragmentation analysis, an effective range of notch lengths and positions relative to the incident bar was identified for achieving optimal fragmentation. The results revealed that a notch length between 0.2 and 0.4 and a notch position between L/2 and 2L/3 from the incident bar (where L equals sample length), produced the most favorable fragment size distribution. These findings can help link laboratory-scale fracture behavior to field-scale rock fragmentation considerations and contribute to a broader understanding of breakage processes in mining engineering.

1. Introduction

Over the years, various investigations have been carried to predict fragment size using different methods. The impacts of a combination of different rock mass properties, blasthole parameters, and powder factor have been used to predict fragment size in various studies [1-6]. The rock mass properties have been given as a rock mass classification entitle "Blastability index (BI)" that is the sum of ratings for five rock mass properties including: rock mass description (RMD), joint plane spacing (JPS), joint plane orientation (JPO), specific gravity influence (SGI) and Mohs hardness (H) [7]. Lilly [7, 8] also used uniaxial compressive strength (UCS) instead of Mohs hardness. BI represents the impact of in-situ rock mass properties on the fragment size of blasted rocks. There has been also a problem associated with the rating of joint plane spacing (JPS) in the BI system given by Lilly, where the rating of joint plane spacing (JPS) has a constant value of 20 for a wide range of JPS between 0.1 to 1 m, a range where joint spacing occurs in the most cases. Hence, the role of JPS as an important parameter affecting the specific charge and the fragment size will be negligible. In a comprehensive actual large-scale study in several geomechanical conditions such as iron ore mine, the real effect of JPS in the combination of blastability index system on the fragment size has been adjusted and the JPS ratings of 20, 30, 40 were found as a better influence of joint plane spacing for three ranges of 0.1 – 0.2, 0.2 – 0.5 and 0.5 –1.0 m respectively [4]. Hole

Corresponding author: vahab.sarfarazi@gmail.com (V. Sarfarazi)

diameter (ϕ_h) or explosive charge per hole (Q) can also be used to represent the impact of the other blasthole parameters on rock fragmentation by blasting, since parameters like burden (B), spacing (S), stemming (S_t), Length of explosive (L_e) and bench height (K) have a good correlation with ϕ_h and Q, as they increase generally with increasing ϕ_h or Q [9, 10].

Considering the above-mentioned studies, it is evident that the quality of blast-induced fragmentation is influenced by several factors, which can be broadly classified into three categories: mechanical and physical characteristics of the rock, blasting method, and blasting parameters [11, 12]. The presence of natural fractures and discontinuities within iron ore rock masses causes the fragment size resulting from blasting operations to be inherently non-uniform. When the fragmented pieces are either excessively large or overly fine, this directly impacts extraction, loading, transportation, and mineral processing costs. For example, in the Galali iron ore mine, under a constant blast-induced impact pressure, the existence of long fractures close to the blast hole wall significantly increases wave attenuation. Consequently, the effectiveness of the blast is reduced, leading to the production of large iron ore fragments after blasting. This issue not only elevates secondary crushing costs but also complicates the handling and transportation of the fragmented material (Figure 1a).

Conversely, when the rock mass contains shorter fractures or fractures located farther from the blast holes, wave attenuation decreases, resulting in an increased effective blasting intensity. Under such conditions, the resulting fragments become significantly finer, causing increased energy loss, flyrock, airblast phenomena, and substantial dust generation (Figure 1b). These phenomena, in addition to exacerbating environmental hazards, can have a notable adverse impact on the mining operational environment and the operating company's public image, which ultimately poses limitations to the sustainable development of iron ore mines. Both scenarios substantially affect the economic and environmental benefits of open-pit mining. Hence, selecting proper blasting parameters and designing an appropriate blast hole pattern can effectively mitigate challenges such as increased secondary crushing costs, difficulties in fragment handling, and dust pollution caused by suboptimal blasting. These improvements ultimately enhance the efficiency of open-pit mining operations.

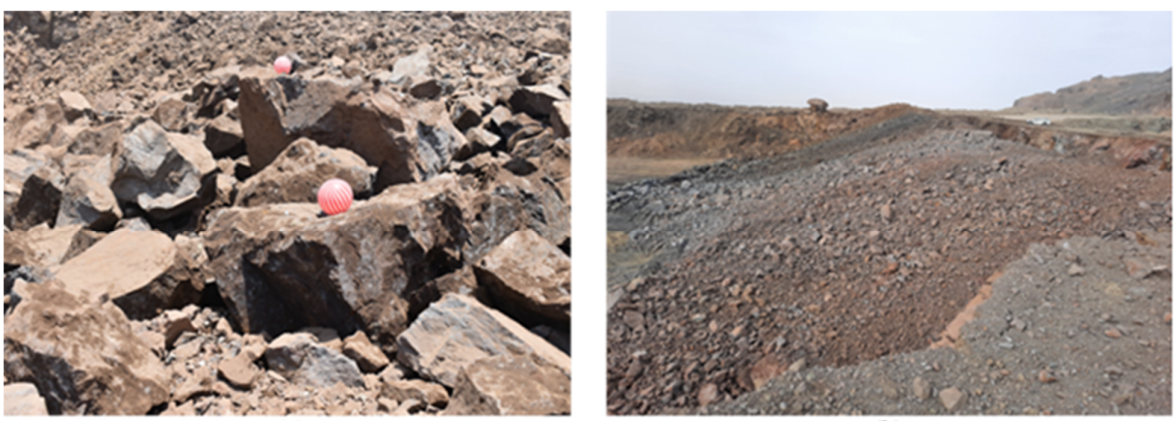

(a) (b)

Figure 1. Galali iron ore mine: (a) Iron ore block with longer fractures located closer to the blast hole wall, (b) Iron ore block with shorter fractures located farther from the blast hole wall.

Joints are common geological structures that markedly influence the mechanical characteristics and engineering conduct of rocks [13,14]. Furthermore, joints have a substantial influence on the mechanical response of rocks, stress wave diffusion, and the fracture mechanism [15–17]. Numerous researchers have previously investigated the effects of rock masses' joints on dynamic mechanical characteristics [18–21] and damage mechanisms [22–25]. The geometric parameters of notches primarily consist of notch roughness, thickness, inclination, and aperture [26,27]. Walton et al. [28] examined the impact of pre-existing notches on fundamental rock mass parameters, including stiffness and peak strength.

The Split Hopkinson Pressure Bar (SHPB) is the most commonly used technique to investigate the mechanical and physical properties of materials under high strain rates [29]. SHPB test is considered a fundamental part of dynamic impact

experiments [30], and it is also widely used in blast engineering applications [31]. The experimental method involves measuring strain on the transmitted and incident bars; these measurements indirectly determine the stress–strain relationship of the specimen. This method is regarded as a simple and indirect approach for conducting dynamic tests [32]. Dai et al. [33] employed the SHPB device to conduct a detailed investigation into the efficacy of protective materials in reducing blast-induced damage to tunnel-surrounding rocks. Shi et al. [34] employed the Split Hopkinson Pressure Bar apparatus to examine the destructive effects of blasts combined with directional shock absorption on rock specimens. Similarly, Geo et al. [35] conducted dynamic impact experiments on rock samples utilizing the SHPB device and quantified the effective energy consumption required for rock fragmentation.

Liu et al. [36], through quasi-rock experiments, examined the influence of joint geometry, joint number, strain rate loading, the properties and thickness of infilled materials, and the geometric proportions of the specimens on the dynamic compressive strength and fracture behavior of jointed rock-like materials. Li et al. [37–39], using SHPB tests on specimens with varying joint roughness, examined the relationship between dissipated energy and the fractal dimension of jointed samples. In addition, Li et al. [40] examined the influence of strain rate and joint inclination on the failure pattern, energy transmission, and energy dissipation law in quasi-rock materials. Yang et al. [41] and Zhang et al. [42] also employed SHPB testing on quasi-rock materials to examine the impact of joint thickness on the dynamic properties of rocks. Ping et al. [43] studied the dynamic mechanical characteristics of sandstone specimens containing pre-existing joints at different inclinations, finding that the most complex fracture geometry occurred at a joint angle of 45°. Wang et al. [44,45] explored the influence of pre-existing notch angles on energy dissipation and wave characteristics in quasi-rock materials.

Du et al. [46] investigated the influence of joint length on the mechanical characteristics of sandstone through high-strain-rate testing with the SHPB apparatus. Their findings revealed that the presence of joints in sandstone leads to an increased plastic deformation ratio in the stress–strain curve. Studies [47–50] comprehensively examined the influence of water content and strain rate during dynamic compression tests on both dry and saturated rocks, with a focus on mechanical characteristics and the crack propagation mechanism. Zhao et al. [51] studied the mechanical characteristics, energy dissipation properties, and failure mechanisms of jointed rock specimens containing pre-existing joints at various angles. You et al. [52] performed dynamic tests on sandstone specimens containing pre-existing joints under varying strain rates and determined that both dynamic strength and energy absorption density increase with increasing strain rate. Malachi et al. [53] examined the effects of increasing strain rate under dynamic compressive loading, revealing that higher strain rates lead to greater joint surface development and increased specific fracture energy during the rock failure process. By converting these findings into dimensionless engineering parameters, the results can be utilized for optimizing rock breakage and reducing energy consumption and loss. Yan et al. [54] analyzed the influence of strain rate on the dynamic behavior of jointed rocks subjected to high-velocity loading, showing that increased strain rate results in enhanced fracturing and higher energy dissipation density. Yin et al. [55] investigated the effects of dynamic impacts on rocks with varying bridge lengths and moisture conditions, revealing that both moisture content and rock bridge length considerably affect the dynamic compressive strength, Young's modulus, and energy absorption density.

In recent years, extensive research has investigated the influence of notch length on the dynamic behavior and fragmentation process of rocks. However, only a limited number of studies have simultaneously considered the combined effects of notch length and various notch positions relative to the incident bar, particularly under conditions representative of open-pit iron ore mining. To address this research gap, the present study conducted high-strain-rate impact testing using the Split Hopkinson Pressure Bar apparatus on iron ore specimens containing pre-existing non-persistent edge notches with varying lengths and positions relative to the incident bar. The experimental results were used to evaluate dynamic mechanical characteristics, failure patterns, fragmentation distribution, and fractal dimension. The main objective of this research is to examine the effects of notch length and position on the dynamic behavior and fragment size distribution of the fragmented iron ore. The findings provide a critical scientific basis for improving blasting parameters in open-pit iron ore mining operations.

2. Materials and Methods

2.1. Specimen Collection and Preparation

The iron ore specimens employed in this study were obtained from the Galali open-pit iron ore mine located in Kurdistan Province. All specimens were cored from a single iron ore block to ensure material homogeneity (Figure 2). Using a core drilling machine, cylindrical specimens with a height and diameter of 22 mm were prepared. During the specimen preparation process, the top and bottom surfaces were carefully ground using a precision grinding machine and subsequently polished with silica powder. All preparation procedures strictly followed the standards set by the International Society for Rock Mechanics (ISRM).

The flatness of the specimen ends was controlled within 0.02 mm, and the deviation from perpendicularity of the end surfaces was limited to a maximum of 8 degrees. A 3 mm-thick diamond wire saw was used to create non-persistent edge notches in the specimens. In total, nine specimens with notch inclination angles of zero degrees were prepared, incorporating three different notch surface-to-total shear surface ratios of 0.2, 0.4, and 0.6, and three different notch positions relative to the incident bar, which were positioned at L/3, L/2, and 2L/3 of the specimen height (Figure 3).

Figure 2. Core drilling process and extracted iron ore core samples

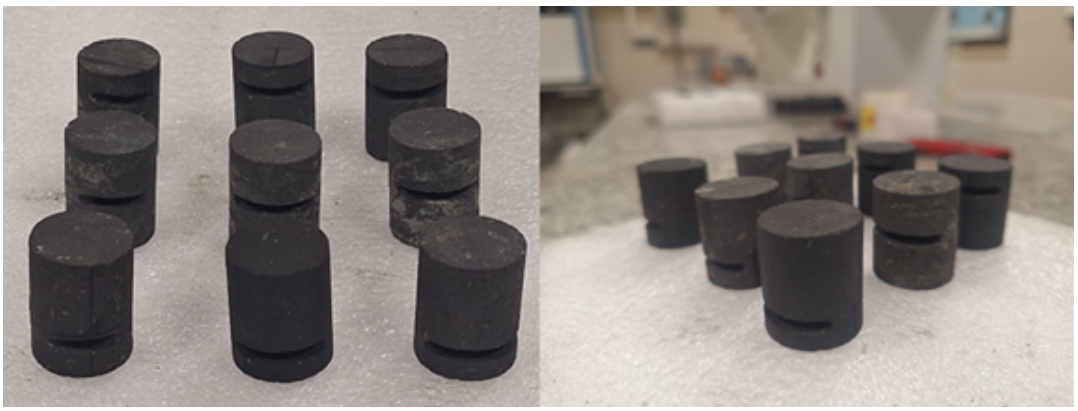

Figure 3. prepared specimens for SHPB tests

2.2. Instruments and equipment

As shown in Figure 4, a Split Hopkinson Pressure Bar (SHPB) apparatus with a bar diameter of 25 mm, located in the Strength of Materials Laboratory at Bu-Ali Sina University, Hamedan, was employed for the experiments. This system comprises four main components: the loading system, the pressure bar system, the energy absorption system, and data analysis and acquisition system. The specimens are placed between the transmission and incident bars. The loading system serves provides the driving force and generates the compressive wave throughout the entire setup. It consists of a compressed-air

reservoir, a pressure gauge, and a striker bar. For the present experiments, a gas pressure of 12.5 MPa was selected, which adequately fulfills the test requirements. The striker bar, made of 40Cr alloy steel, has a diameter of 25 mm and a length of 500 mm.

The pressure bar system consists of transmission and incident bars, both fabricated from the same material as the striker bar. Each of the transmission and incident bars measures 2000 mm in length and 25 mm in diameter. The bars have a density of 7850 kg/m³, an elastic modulus of 210 GPa, and a longitudinal wave speed of 5180 m/s.

The energy absorption system is designed to dissipate the residual energy in the transmission bar and consists of an absorbing bar and a buffer unit. The data acquisition and analysis system record the transmitted, reflected, and incident wave signals through a data logging system. To extract the mechanical characteristics of the rock specimens, two data processing steps are required: first, filtering the raw signals to eliminate noise, and second, calculating the specimens' dynamic properties.

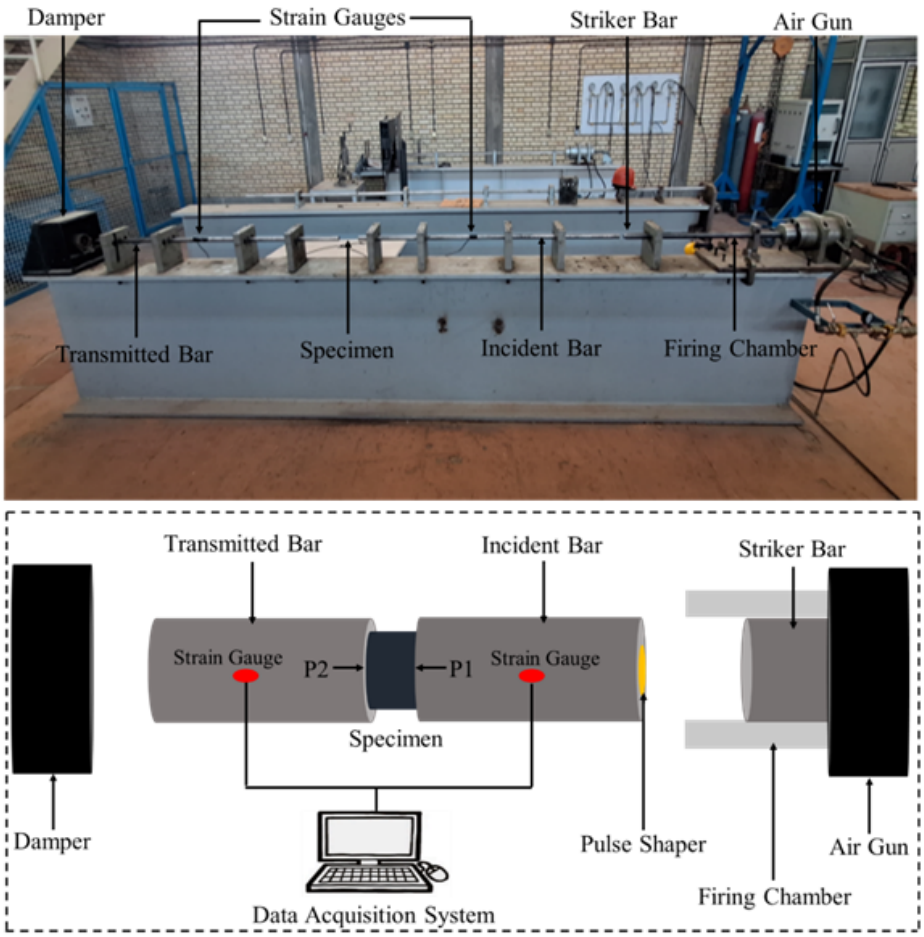

Figure 4. Photograph and schematic of the SHPB apparatus

2.3. Test Method

During the experiment, the striker bar is propelled by compressed gas and impacts the incident bar, initiating a compressive wave. This compressive wave then propagates along the incident bar toward the specimen. Upon reaching the specimen–bar interfaces, the compressive wave is partially transmitted into the specimen and partially reflected. Multiple transmissions and reflections arise at the interface of the specimen and bars, inducing high strain-rate deformation in the specimen. Simultaneously, a segment of the compressive wave is reflected back toward the incident bar, while another portion is transmitted through the iron ore specimen and enters the transmission bar, forming the reflected and transmitted wave signals, respectively. These signals are recorded by strain gauges mounted on

both the transmission and incident bars, allowing for the measurement of the incident (ε_I), reflected (ε_R), and transmitted (ε_T) strains in the specimen.

Based on the guidelines provided by the ISRM for dynamic mechanical testing of rocks, an effective test must fully establish dynamic stress equilibrium conditions:

$$\sigma_1 = \sigma_2 \quad (1)$$

σ_1 and σ_2 represent the stresses exerted at both ends of the rock specimen, respectively. That is to say, all points within the specimen must meet the following stress equilibrium condition:

$$\varepsilon_I(t) + \varepsilon_R(t) = \varepsilon_T(t) \quad (2)$$

where $\varepsilon_I(t)$, $\varepsilon_R(t)$, $\varepsilon_T(t)$ denote the incident, reflected and transmitted wave strains, respectively.

Furthermore, the validity and reliability of the SHPB test primarily rely on the assumptions of uniaxial stress wave propagation and stress uniformity inside the specimen. Therefore, before performing dynamic impact tests, it is essential to verify that stress equilibrium is established stress equilibrium throughout the loading process to guarantee the precision of the obtained data [56].

The dynamic stress equilibrium condition was assessed by analyzing the transmitted, reflected, and incident wave signals acquired from uniaxial dynamic compression test to verify the reliability of the testing apparatus. As depicted in Figure 5, the stress-time curves corresponding to the incident wave (In), transmitted wave (Tr), and reflected wave (Re) are shown. The sum of the reflected and incident strains coincides with the transmitted strain, indicating that the specimen-maintained stress equilibrium during the dynamic loading process.

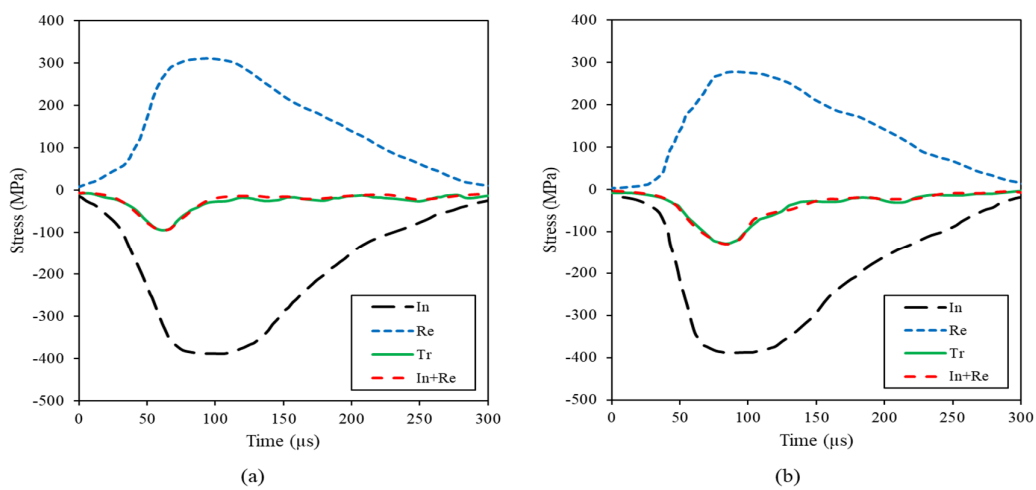

Figure 5. Investigation of dynamic stress equilibrium in iron ore specimens with varying notch lengths and positions relative to the incident bar: (a) notch surface/ total shear surface = 0.6 and notch position / specimen length = L/3 (S3); b) notch surface/ total shear surface = 0.6 and notch position / specimen length = 2L/3 (S9).

As a result, the dynamic compressive strength and strain of the tested samples were determined using the three-wave analysis method. The corresponding equations are presented below:

$$\begin{cases} \sigma_S = \dfrac{P_1 + P_2}{2A_S} = \dfrac{AE}{2A_S}(\varepsilon_I + \varepsilon_R + \varepsilon_T) = \dfrac{AE}{A_S}\varepsilon_T \\ \varepsilon = \dfrac{C_0}{L_0}\displaystyle\int_0^t (\varepsilon_I - \varepsilon_R - \varepsilon_T)\,dt = -\dfrac{2C_0}{L_0}\int_0^t \varepsilon_R dt \\ \dot{\varepsilon} = \dfrac{C_0}{L_0}(\varepsilon_I - \varepsilon_R - \varepsilon_T) = -\dfrac{2C_0}{L_0}\varepsilon_R \end{cases} \quad (3)$$

where σ_S denotes the stress applied to the specimen, A_S corresponds to the specimen's cross-sectional area, and L_0 indicates its original length. Based on these parameters, the stress–strain curve of the specimen at the strain rate $\dot{\varepsilon}$ can be calculated and extracted.

3. Results

3.1. Stress–Strain Curve

Utilizing the transmitted, reflected, and incident wave data, the stress–strain curves of each iron ore specimen under dynamic compressive loading were derived using the three-wave analysis method. Figure 6 presents the stress–strain curves of the specimens under dynamic compressive loading at a constant strain rate, considering different notch lengths and positions relative to the incident bar. The

results indicate that, under identical loading circumstances, the peak stress in the stress–strain curve increases as the notch length decreases and the notch distance from the incident bar increases.

The stress–strain curves can generally be categorized into four stages: (I) compression of cracks, (II) linear deformation of the rock, (III) rock yielding, and (IV) final fracture of the rock. In the first stage, known as crack compression, naturally existing microcracks and fractures in the microstructure of the iron ore specimens begin to close as the compressive load is applied. During the second phase, known as the linear deformation region, the stress–strain curve increases almost linearly. The slope of this region is defined as the dynamic elastic modulus of the specimen. In the third phase, as the stress increases, the stress–strain curve gradually deviates from linearity and enters the yielding region. During this phase, localized fractures begin to propagate within the specimen; cracks coalesce and eventually result in the growth of primary cracks and the initiation of new cracks. The fourth stage begins once the maximum stress is reached, where stress suddenly reduces, indicating the onset of the specimen's final failure process. The stress–strain behavior in this stage is strongly influenced by the notch length and position within the specimen, and its variations can serve as indicators of the material's strength and failure mechanisms under dynamic loading situations.

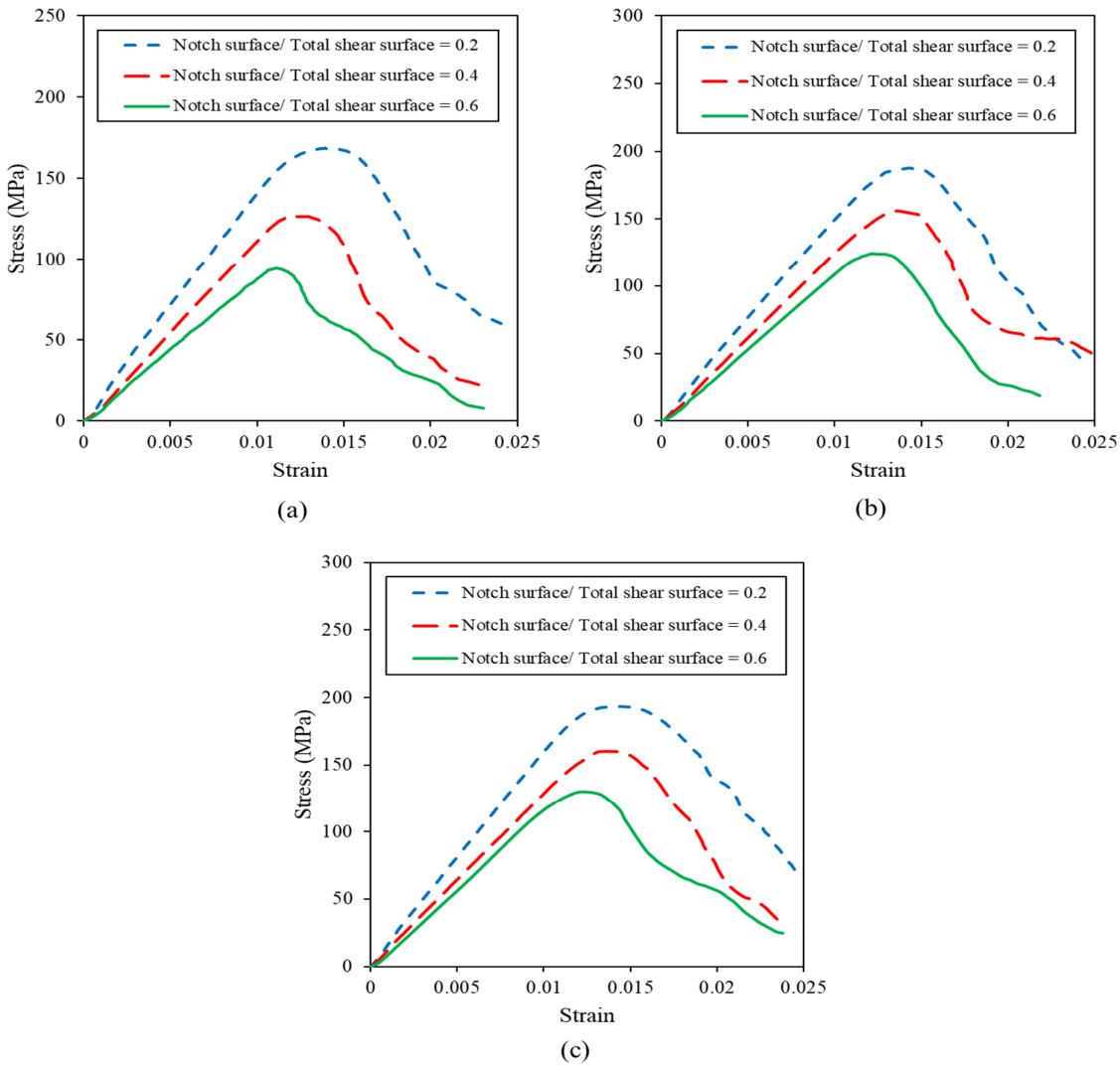

Figure 6. Dynamic stress–strain curves of rock specimens with different notch lengths and positions relative to the incident bar: (a) notch position / specimen length = L/3 and notch surface/ total shear surface = 0.2, 0.4 and 0.6; (b) notch position / specimen length = L/2 and notch surface/ total shear surface = 0.2, 0.4 and 0.6; (c) notch position / specimen length = 2L/3 and notch surface/ total shear surface = 0.2, 0.4 and 0.6.

3.2. Dynamic Compressive Strength

Dynamic compressive strength is a critical parameter for evaluating the mechanical characteristics of rocks under high strain rate loading. Figure 7 depicts how the dynamic compressive strength of iron ore specimens varies with different notch lengths and positions relative to the incident bar. It is evident that, when the notch length is held constant, the dynamic compressive strength of the specimens increases in an almost linear manner as the notch distance from the incident bar increases. This phenomenon is mainly due to the fact that when the notch is positioned farther from the wave entry source (incident bar), the compressive wave travels a longer distance within the specimen before reaching the notch. As a result, less energy is reflected at the notch, allowing a greater portion of the incident wave energy to be absorbed by damage mechanisms, including crack propagation, fragmentation, and internal structural failure of the specimen. This results in a significant improvement in the dynamic compressive strength of the specimen under these conditions.

Also, when the notch position relative to the incident bar is held constant, the dynamic compressive strength of the specimens decreases linearly with increasing notch length. This phenomenon happens because, as the notch length increases, the extent of discontinuities along the wave propagation path also increases. Consequently, the impact wave interacts with a larger discontinuity surface, leading to significant reflection and scattering of the incident wave energy. Additionally, internal friction between the notch surfaces increases, causing a greater portion of the energy to be dissipated as heat and localized deformation along the notch interface. Overall, longer notches act as more effective barriers to dynamic energy transmission, resulting in reduced energy transfer to the intact regions of the specimen and ultimately mitigating the extent of failure and crack propagation.

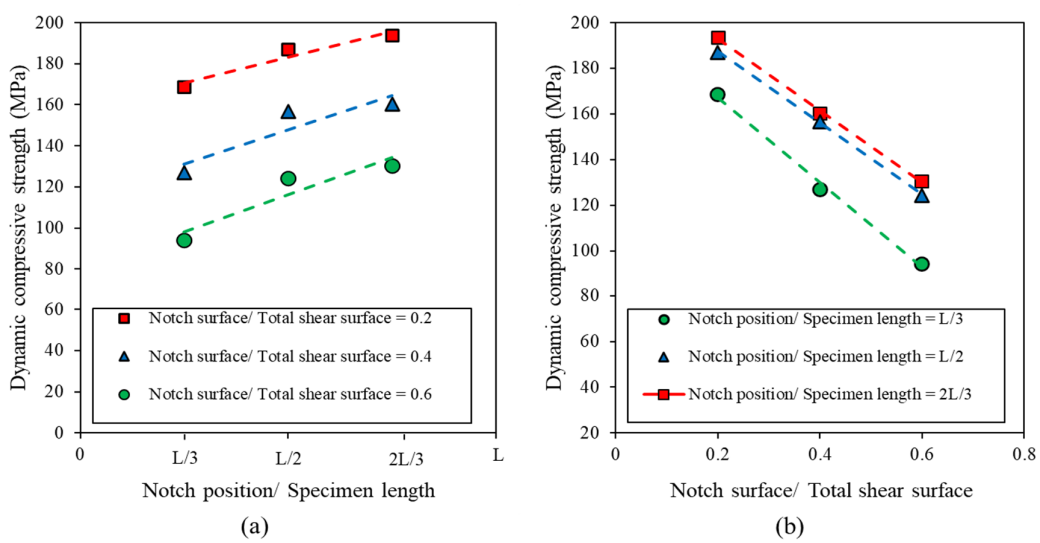

Figure 7. Dynamic compressive strength and corresponding fitted curves for specimens subjected to variations in notch length and position relative to the incident bar: (a) different notch positions; (b) different notch lengths.

3.3. Dissipated Energy

In dynamic experiments, the entire system operates in accordance with the principle of energy conservation. In the Split Hopkinson Pressure Bar (SHPB) test, the total system energy can be divided into four main components: the incident energy (U_I), the transmitted energy (U_T), the reflected energy (U_R), and the energy delivered to the specimen, referred to as the specimen's absorbed energy (U_S):

$$\begin{cases} U_I(t) = \dfrac{A_0C_0}{E}\int \sigma_I^2(t)dt = A_0C_0E\int \varepsilon_I^2(t)dt \\ U_R(t) = \dfrac{A_0C_0}{E}\int \sigma_R^2(t)dt = A_0C_0E\int \varepsilon_R^2(t)dt \\ U_T(t) = \dfrac{A_0C_0}{E}\int \sigma_T^2(t)dt = A_0C_0E\int \varepsilon_T^2(t)dt \end{cases} \quad (4)$$

where E, C_0, and A_0 denote the elastic modulus, the velocity of the longitudinal wave, and the cross-sectional area of the incident bar (or transmission bar), respectively. Based on the principle of energy

conservation, the energy absorbed by the specimen (U_s) can be expressed as:

$$U_S = U_I - (U_R + U_T) \quad (5)$$

Earlier research has demonstrated that the majority of the energy input to the specimen, particularly under dynamic loading conditions, is consumed by internal processes such as deformation, the onset and growth of cracks, and eventual failure. It has been reported that approximately 95% of the total energy imparted to the specimen is dissipated within it [57]. Therefore, the energy absorbed by the specimen may be regarded as a valid approximation of the dissipated energy (U_d):

$$U_d = U_s \quad (6)$$

Figure 8 illustrates the changes in the dissipated energy of the specimens as a function of different notch lengths and positions relative to the incident bar. The findings reveal that, under consistent loading conditions, the dissipated energy in the specimens increases approximately linearly with decreasing notch length and increasing notch distance from the incident bar.

Based on the experimental findings and analyses, it is observed that when the notch length is held constant, increasing the notch distance from the incident bar results in the stress wave traveling a longer path inside the specimen before reaching the notch. This extended wave propagation path reduces the initial energy loss due to reflection at the notch, resulting in a greater portion of the incident wave energy being used for crack propagation and causing more severe damage to the specimen's internal structure. Ultimately, this phenomenon leads to increased energy dissipation through localized failure processes, crack extension, and final specimen fracture.

Conversely, when the notch position relative to the incident bar is held constant, increasing the notch length leads to a significant decrease in the specimen's resistance to fracture. In other words, longer notches possess a lower capacity for absorbing the applied energy; consequently, the quantity of energy absorbed in by the specimen decreases, leading to a more rapid failure process.

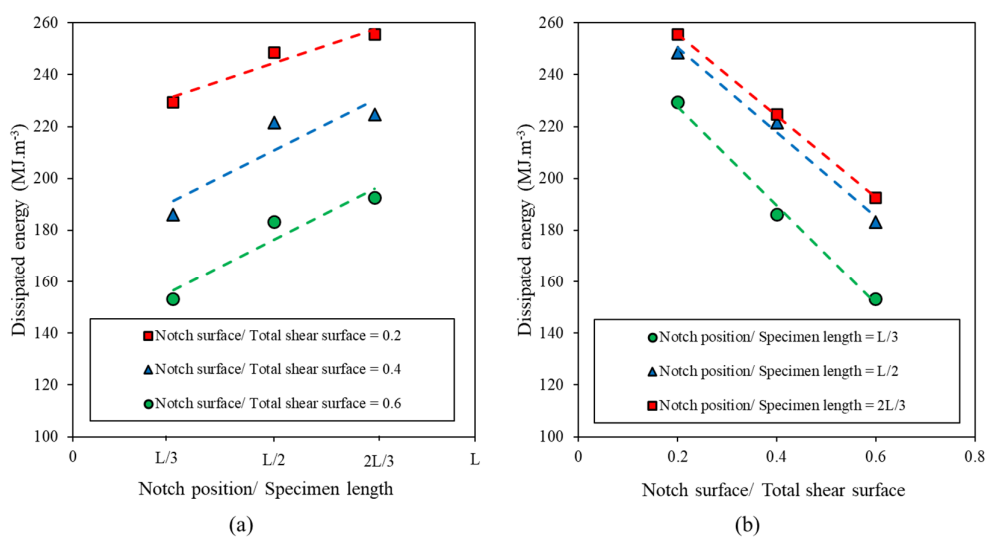

Figure 8. Dissipated energy of the specimens and their fitted curves under the influence of notch length and position relative to the incident bar: (a) different notch positions; (b) different notch lengths.

3.4. Dynamic Compressive Strength versus Dissipated Energy

Dynamic compressive strength is a critical parameter for describing the mechanical characteristics of rocks under high strain-rate loading and serves as a key indicator to assess the extent of damage and failure in rock materials. Additionally, rock fragmentation has a direct influence on the amount of energy dissipated within the specimen. Therefore, dynamic compressive strength can serve as a criterion for describing and predicting the energy dissipated in rock materials. As shown in Figure 9, the dissipated energy increases with increasing dynamic compressive strength, following a distinct trend. The equation below, derived from fitting the experimental results, represents the correlation between the dynamic compressive strength and the dissipated energy in the iron ore specimens:

$$U_d = -9 \times 10^{-4}\sigma^2 + 1.2951\sigma + 38.003 \quad (7)$$

where U_d refers to the dissipated energy and σ stands for the dynamic compressive strength.

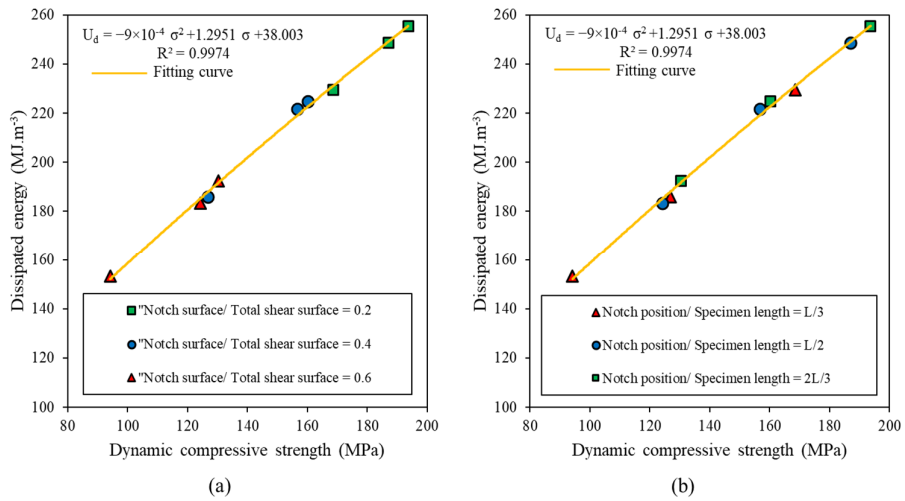

Figure 9. Dissipated energy versus dynamic compressive strength: (a) different notch positions; (b) different notch lengths.

Throughout the failure process, the rock must continuously absorb energy to create the necessary conditions for the initiation and propagation of internal cracks. When the absorbed energy attains a critical threshold, failure occurs; the rock sustains damage, and some of the energy is dissipated. This point typically coincides with the specimen reaching its dynamic compressive strength. For a rock with a defined level of internal damage subjected to a given external force, the energy required to reach the predetermined failure threshold is fixed. Therefore, it can be concluded that there is a significant and systematic correlation between the absorbed energy and the dynamic compressive strength of the rock, which could serve as a fundamental basis for analyzing the mechanical properties of rock under dynamic loading conditions.

3.5. Failure Pattern of Specimen

Figure 10 illustrates three specimens containing non-persistent edge notches, each with a notch angle of 0°, located at a distance of L/3 from the incident bar, and having notch surface-to-total shear surface ratios of 0.2, 0.4, and 0.6. Examination of the fracture surface of specimen S1 indicates the formation of an irregular failure cone at the impact site. The maximum depth of this cone was measured to be 4.4 mm, corresponding to 0.2 times the specimen height (22 mm). At the location of the cone formation, shear cracks developed, as evidenced by the observation that the bottom surface of the cone was rough and undulated, containing angular fragments, characteristic of shear fractures. Also, tensile cracks propagated vertically relative to the specimen axis at the lower part of the cone and connected to the specimen's bottom surface. The fracture surfaces resulting from these tensile cracks were smooth and polished, which is a typical feature of tensile fractures. Beneath the failure cone, irregularly shaped blocky chips were formed. Additionally, large-scale shear cracks originated from the notch tip and propagated obliquely at an angle of 65 degrees relative to the vertical axis, extending opposite to the y-axis direction and connecting to the specimen's end. Blade-shaped conical chips formed along the specimen's wall, while smaller fragments developed in the central region, extending from beneath the cone to the top of the lower wedge-shaped section. The height of the blade-shaped conical region was estimated to be approximately 0.75 times the specimen height. The size of the fragments beneath the blade-shaped cone gradually decreased toward the specimen's end.

Furthermore, the fracture surface analysis of specimen S2 reveals that four primary radial cracks originated from the top surface and branched toward the specimen's lateral boundaries. These cracks propagated through the entire specimen height and connected to the bottom surface. Additionally, the presence of foliation planes in the specimen induced stress concentration, leading to

the formation of tensile cracks along these discontinuities. Incomplete blade-shaped conical chips are also clearly visible along the specimen's lateral wall. Moreover, large-scale shear cracks extended obliquely from the notch tip at an angle of 55 degrees relative to the vertical axis, propagating opposite to the y-axis direction and connecting to the specimen's end.

In specimen S3, fracture surface analysis reveals that four primary radial cracks, shaped like an hourglass or an X, originated from both ends of the specimen and branched toward the side boundaries. The fracture surface examination indicated the presence of small-scale shear cracks beneath the striker, which were clearly visible. Large-scale shear cracks also propagated from the notch tip, growing obliquely at an angle of 46 degrees relative to the vertical axis, extending opposite to the y-axis direction and connecting to the specimen's end. Due to the considerable notch length in this specimen, wave attenuation was significant to the extent that the impact energy did not transmit to the lower parts of the notch, resulting in the formation of a large-scale wedge in the upper section of the specimen. Similar to previous configurations, the shapes of the fragments formed along the specimen's boundaries exhibited blade-shaped conical geometries, with their sizes gradually decreasing from the impact site toward the specimen's end. Examination of the notch surface showed no damage to the lower surface of the notch, with no cracks observed in this region. Under these conditions, the upper regions of the notch primarily experienced shear failure, while the lower regions were predominantly subjected to tensile failure.

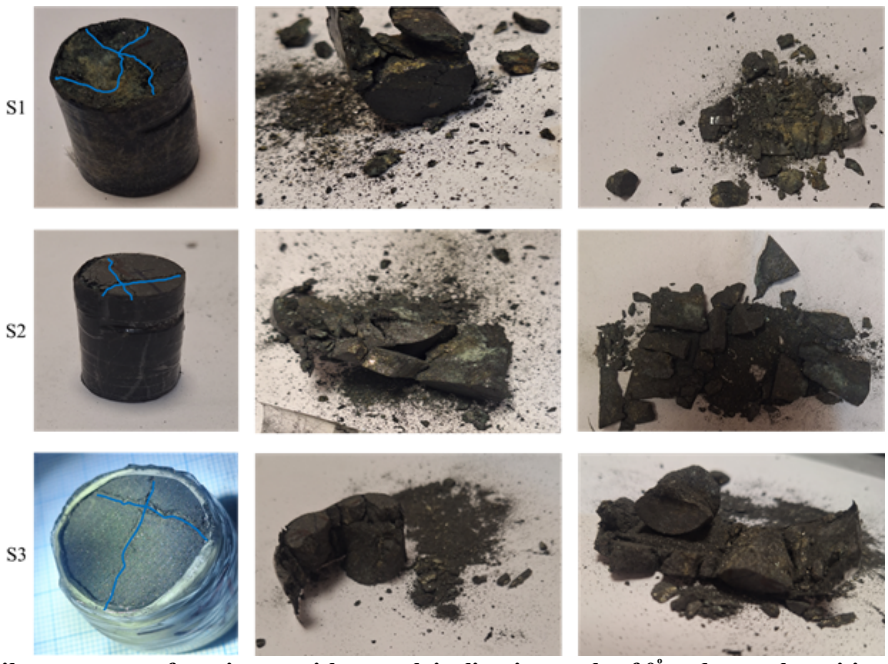

Figure 10. Failure patterns of specimens with a notch inclination angle of 0° and a notch position at L/3 of the specimen length relative to the incident bar: (S1) notch surface/ total shear surface = 0.2; (S2) notch surface/ total shear surface = 0.4; (S3) notch surface/ total shear surface = 0.6.

Figure 11 illustrates three specimens containing non-persistent edge notches, each with a notch angle of 0°, located at a distance of L/2 from the incident bar, and having notch surface-to-total shear surface ratios of 0.2, 0.4, and 0.6. The fracture surface analysis of specimen S4 reveals the formation of branched or multi-pronged cracks. The study shows that shear cracks initiated beneath the striker and propagated obliquely up to about 0.5 mm. Additionally, other shear cracks with rough surfaces originated from the specimen's top surface at an angle of 69 degrees relative to the vertical axis and extended to the notch. This crack propagation pattern resulted in the formation of a rock wedge. In this configuration, irregular blocky wedges formed around the specimen, with their size reducing as the distance from the impact site increases. The central wedges on the upper and lower faces of the specimen are approximately equal in size, indicating the validity of the results, as the specimen's symmetry about the central notch led to the formation of similarly sized wedges on both surfaces.

Subsequently, the fracture surface analysis of specimen S5 indicates the formation of branched cracks on both the upper and lower faces of the specimen. In the region beneath the striker, the cracks are predominantly shear in nature and have propagated up to approximately half a millimeter. These shear cracks produced pulverized material and rough surfaces along the specimen's upper wall. From the specimen surface, shear cracks developed obliquely at an angle of 61 degrees relative to the vertical axis, extending toward the notch tip and eventually connecting with each other. This progression led to the formation of a rock wedge on the specimen's upper surface. The stress transmitted from the tip of the upper wedge to the lower notch surface caused the development of a shear wedge on the specimen's bottom surface. At the interface between these two wedges, pulverized material and fine fragments with rough surfaces were observed, indicative of shear failure in this region. Around the specimen, incomplete blade-shaped conical wedges were also formed, with the size of these fragments gradually decreasing from the specimen's front to its end.

Therefore, the fracture surface analysis of specimen S6 reveals the presence of four main cracks arranged in a pattern resembling an hourglass or an X shape, branching out on both ends of the specimen. A detailed examination of the fracture surface indicates that small-scale shear cracks formed beneath the striker and propagated obliquely over a distance of approximately three millimeters. Additionally, large-scale shear cracks originated from the tip of the pre-existing notch and extended toward the specimen's end at an angle of approximately 58 degrees relative to the vertical axis, eventually connecting to the specimen boundary. Due to the considerable notch length, wave attenuation significantly increased, such that the impact energy did not transmit to the lower regions of the notch. This resulted in the formation of large-scale rock wedges in the upper region of the specimen. Consistent with previous configurations, the fragments formed along the specimen edges exhibited blade-shaped conical wedges, with their dimensions gradually decreasing from the impact site toward the specimen's end.

Overall, the generated fragments, particularly the central fragment in the lower region of the specimen, exhibit larger dimensions compared to other central fragments extending in different directions. Furthermore, the examination of the notch surface reveals that no damage or cracking has propagated to the lower surface of the notch. Therefore, the upper regions of the notch predominantly experienced shear failure mechanisms, while the downstream lower regions primarily underwent tensile failure mechanisms.

Figure 11. Failure patterns of specimens with a notch inclination angle of 0° and a notch position at L/2 of the specimen length relative to the incident bar: (S4) notch surface/ total shear surface = 0.2; (S5) notch surface/ total shear surface = 0.4; (S6) notch surface/ total shear surface = 0.6.

Figure 12 illustrates three specimens containing non-persistent edge notches, each with a notch angle of 0°, positioned at a distance of 2L/3 from the incident bar, and having notch surface-to-total shear surface ratios of 0.2, 0.4, and 0.6. The fracture surface examination of specimen S7 reveals three primary radial cracks originating from the specimen center and extending toward its lateral boundaries at approximately 120-degree angles relative to each other. Additionally, branching cracks originate from the tips of the main fractures. The presence of irregular blocky fractures on the specimen walls is notable. The rough surfaces formed on the specimen walls indicate the presence of shear cracks. The chip formed on the lower surface of the specimen exhibits a blade-shaped conical geometry with a smooth and polished surface. The smoothness and polished of the chip surface indicate the occurrence of tensile fracture in this region.

Also, the fracture surface analysis of specimen S8 indicates that the branching cracks predominantly extend on the upper surface of the specimen, whereas four intersecting cracks have formed on the lower surface. Additionally, secondary branches have propagated from the tips of these main cracks. In this configuration, incomplete blade-shaped conical fractures are observed along the specimen boundaries. It is noteworthy that shear cracks have also developed in the region beneath the striker.

Subsequently, the fracture surface analysis of specimen S9 reveals that tensile branching cracks have formed at the center of the specimen's surface and have propagated radially outward in a branched pattern. On the opposite surface, branching cracks also exhibit radial growth. Additionally, circumferential cracks are observed. Here, circumferential cracks refer to those that develop in a circular pattern around the specimen, while radial cracks are those emanating from the specimen center. In this configuration, blade-shaped conical fractures have formed along the specimen boundaries.

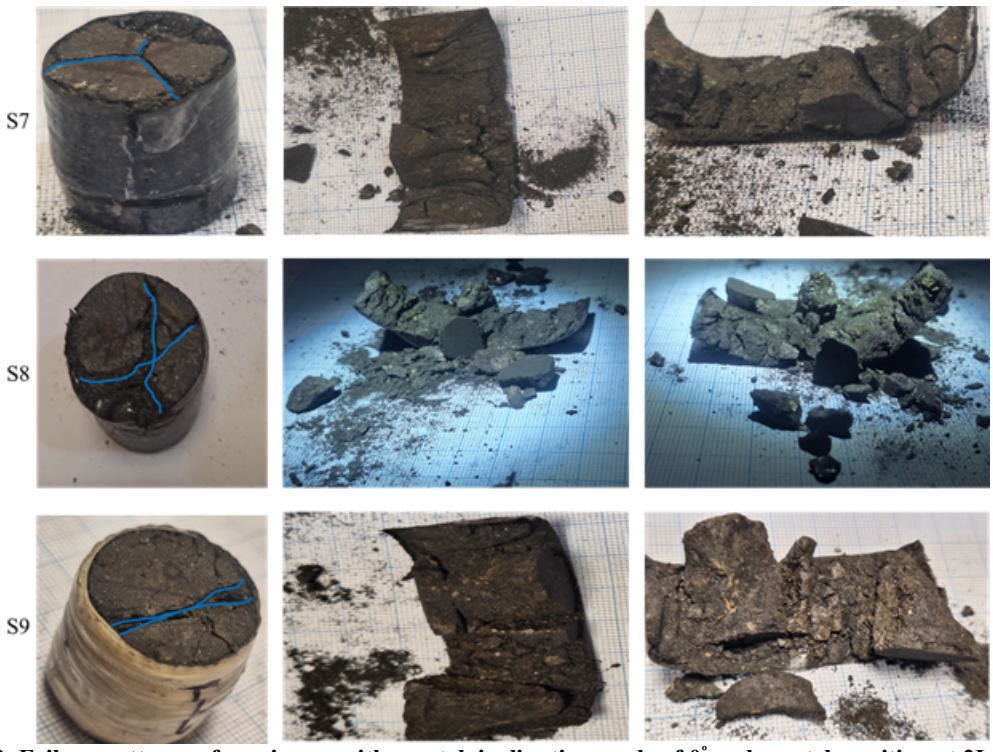

Figure 12. Failure patterns of specimens with a notch inclination angle of 0° and a notch position at 2L/3 of the specimen length relative to the incident bar: (S7) notch surface/ total shear surface = 0.2; (S8) notch surface/ total shear surface = 0.4; (S9) notch surface/ total shear surface = 0.6.

By comparing the specimens presented in Figures 10, 11, and 12, it can be concluded that when the notch position relative to the incident bar is held constant, an increase in notch length leads to the formation of larger intact rock blocks. This can be attributed to the greater wave attenuation caused by longer notches, which reduces the transmitted wave energy and consequently leads to less fragmentation. The fragments resulting from failure around the specimens transition from

irregular blocky shapes to incomplete blade-like cones, and eventually to complete blade-like cones as the notch length increases. In other words, it can be argued that increasing the notch length weakens the impact wave energy, resulting in less wave energy to reach the lower part of the notch. This reduction leads to decreased fragmentation and the formation of larger rock fragment sizes.

Conversely, in specimens with shorter notches, a greater fraction of the wave energy is transmitted to the lower notch region, resulting in increased fragmentation and, consequently, the production of smaller fragments. Fracture surface analysis revealed that the number of shear and tensile cracks in the specimen with a 0.2 notch length is significantly higher than in the specimen with a 0.6 notch length. This phenomenon is attributed to greater wave attenuation in specimens with longer notches. As wave energy decreases, peripheral fractures mainly compressive in nature and requiring substantial energy to form are reduced. From the observed failure patterns associated with the notches, it can be inferred that increasing notch length reduces the angle of the fracture cone surface compared to that of the vertical axis, while simultaneously increasing the height of this cone beneath the notch. Concurrently, as notch length increases, the degree of fragmentation decreases, and the resulting fragments tend to be larger in size.

Additionally, by comparing specimens with identical notch lengths, it can be observed that increasing the distance of the notch position from the incident bar leads to a reduction in the size of the failure fragments surrounding the specimen and an increase in the angle of the fracture cone surface compared to that of the vertical axis. Also, the dimensions of the resulting rock fragments decrease, indicating an increase in fragmentation. This phenomenon occurs because, when the notch is positioned closer to the impact point, a larger portion of the stress wave energy is dissipated throughout the initial stages, leaving only a small fraction to be transmitted to the regions beneath the notch. Consequently, the amount of fracturing in the lower part of the notch decreases, leading to the formation of larger rock blocks and the development of a fracture cone in the area below the notch.

Conversely, as the notch distance from the striker impact point increases, the stress wave induces damage and fragmentation in the upper regions of the rock before reaching the notch location. The remaining portion of this wave, having passed through the rock area opposite the notch, is transmitted to the lower section of the notch and causes its failure; however, in this scenario, a fracture cone does not form. The main reason for the absence of a fracture cone is the limited thickness of the rock section beneath the notch, which causes the transmitted stress wave to be completely attenuated within this region, leading to the overall failure of the entire rock section below the notch. Ultimately, regardless of notch length or its distance from the incident bar, the observed fracture pattern in the specimens consistently exhibits an X-shaped configuration.

3.6. Properties of the distribution of impact fracture fragments in iron ore specimens

The fragmentation characteristics of the iron ore samples were evaluated using the direct sieving technique. As illustrated in Figure 13, the sieves used in this study had mesh sizes with apertures of 22, 12.5, 4.76, 4, 2.38, 1.68, 1.41, and 1 mm. Accordingly, the fragments resulting from the sample comminution were classified into eight size groups: 22 to 12.5 mm, 12.5 to 4.76 mm, 4.76 to 4 mm, 4 to 2.38 mm, 2.38 to 1.68 mm, 1.68 to 1.41 mm, 1.41 to 1 mm, and smaller than 1 mm. This classification considers the 22 mm size as representing the intact iron ore sample prior to comminution. These eight groups were assigned particle size indices i = 1, …, 8 in ascending order of size.

The samples obtained from the experiments, consisting of fragmented pieces with different notch lengths and positions relative to the incident bar, were classified using standard sieves, and the mass of each size fraction was measured individually. The results are presented in Figures 14 to 16. In each chart, the first row represents gradations i = 1 to 4, arranged from right to left, whereas the subsequent row represents the gradations i = 5 to 8, also arranged from right to left.

In general, the results indicate that with decreasing notch length and increasing its distance from the incident bar, the mass percentage of fragments with large diameters reduces, while that of fine fragments increases significantly. This trend reflects an intensification of fragmentation severity in the iron ore samples under these conditions. In other words, a shorter notch leads to greater stress concentration at the tip of the crack, triggering failure, whereas increasing the notch distance from the incident bar allows the stress wave more time to propagate and distribute energy throughout the specimen. This, in turn, activates a broader range of fracture mechanisms and promotes the

propagation of secondary cracks in various regions. Collectively, these two factors enhance the damage extent and fragmentation intensity, resulting in a larger volume of fine particles generated during the failure process.

Fieger 13. Grading sieves used for fragment size analysis after impact crushing.

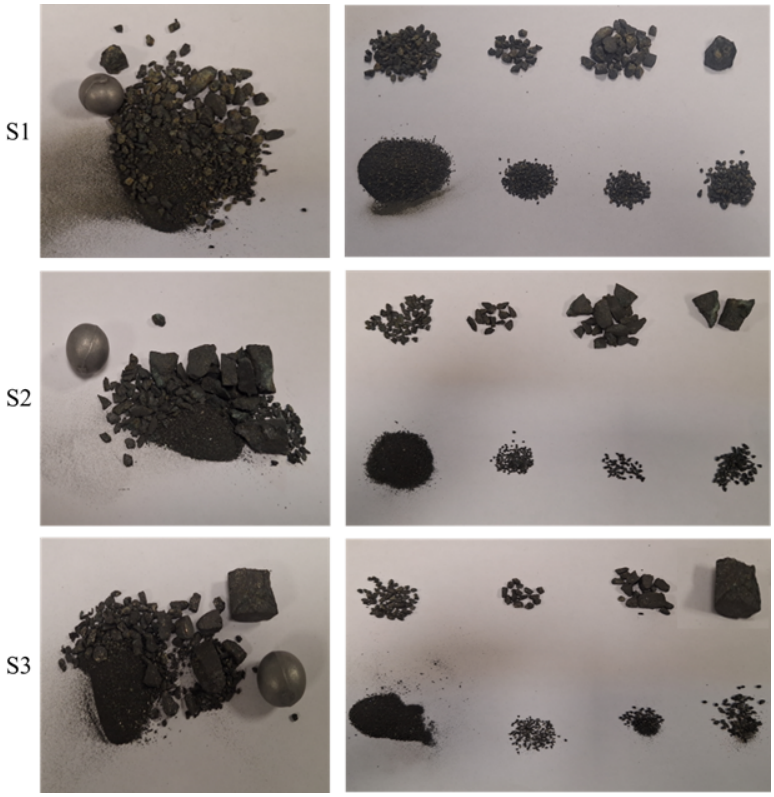

Figure 14. Characteristics of fragmented pieces from iron ore specimens with a notch position at L/3 of the specimen length relative to the incident bar and different notch lengths: (S1) notch surface/ total shear surface = 0.2; (S2) notch surface/ total shear surface = 0.4; (S3) notch surface/ total shear surface = 0.6.

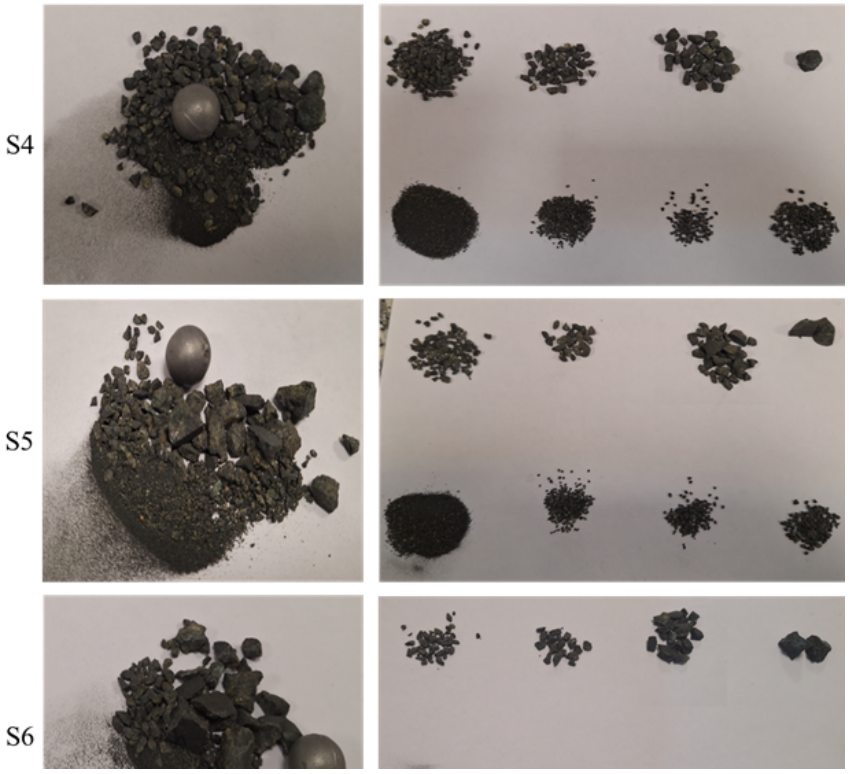

Figure 15. Characteristics of fragmented pieces from iron ore specimens with a notch position at L/2 of the specimen length relative to the incident bar and different notch lengths: (S4) notch surface/ total shear surface = 0.2; (S5) notch surface/ total shear surface = 0.4; (S6) notch surface/ total shear surface = 0.6.

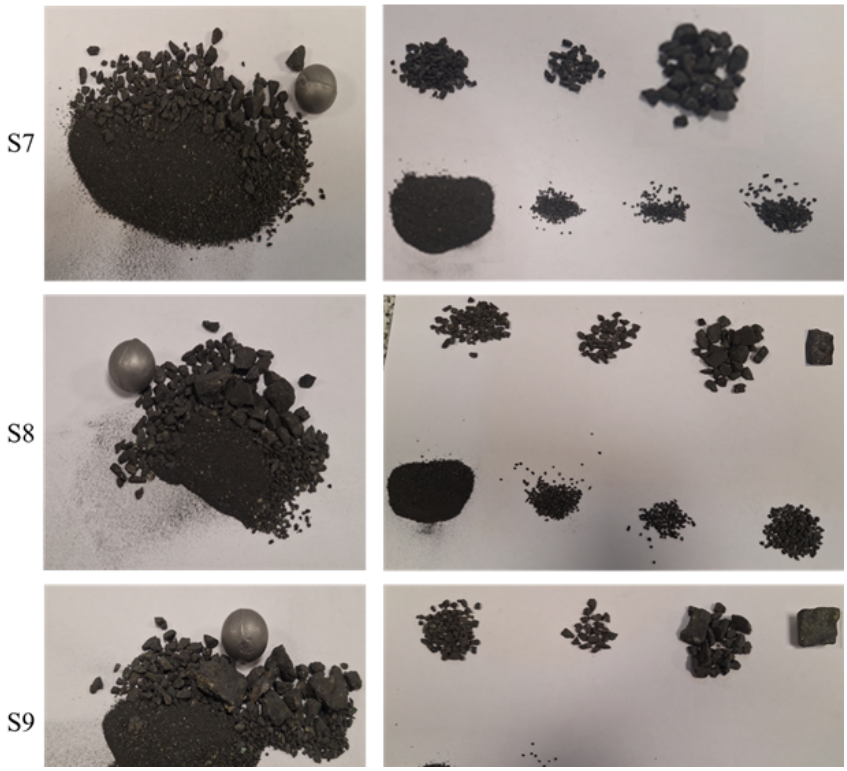

Figure 16. Characteristics of fragmented pieces from iron ore specimens with a notch position at 2L/3 of the specimen length relative to the incident bar and different notch lengths: (S7) notch surface/ total shear surface = 0.2; (S8) notch surface/ total shear surface = 0.4; (S9) notch surface/ total shear surface = 0.6.

After the sieving process, the mass percentage of the fragments was used as a key parameter for analyzing the fragmentation distribution. In other words, the ratio of the mass percentage of each size class of the crushed fragments to the total mass of the original iron ore sample was considered an index for evaluating the degree of sample breakage under different notch lengths and positions relative to the incident bar. In the present research, the average particle size was used as the main indicator for fragmentation analysis. The calculation procedure for this index is described as follows:

First, the fragmented iron ore particles were sieved using a set of standard mesh sieves, and the mass of each size fraction, denoted as m_{di}, was measured using a highly accurate digital balance. Next, the mass percentage of each size group, m_{vi} , was calculated by dividing the mass of that group, m_{di} , by the total mass of the initial sample, m, and then multiplying by 100. Then, the particle size ratio of that group within the entire sample δ_{iv}, is calculated by multiplying the mass percentage of that group m_{vi}, by the mean fragment size of that group d_{iv}. Ultimately, the mean fragment size of the sample under the specified crack length and position relative to the incident bar is obtained by summing the particle size ratios of all groups.

$$\delta = \sum_{1}^{i} \delta_{iv} = \sum_{1}^{i} m_{iv} d_{iv} \quad (8)$$

In this context, the symbol i represents the size group number, resulting from the sieving process, and d_{iv} denotes the mean fragment size of that group, defined as the mean of the minimum and maximum fragment sizes within group i. For example, when i=1, the mean fragment size is 17.25 mm.

After performing the sieving process and initial calculations, the mass percentage and mean fragment size were determined for samples with different notch lengths and positions relative to the incident bar. According to the data presented in Table 1, m denotes the initial mass of the sample, and m_{iv} represents the mass percentage corresponding to the size group i. Figure 17 illustrates the fragment size distribution and the variation in average particle size as functions of different notch lengths and positions under dynamic loading conditions.

As shown in Table 1 and Figure 17, both the length and the position of the notch relative to the incident bar exert a substantial influence on fragment size distribution and the mean fragment size of the iron ore samples.

Table 1. Characteristics of fragmentation distribution in iron ore specimens under different notch lengths and positions relative to the incident bar.

Specimen No.	Notch position	notch length	m(g)	m_{iv} (%)								Mean fragment size (mm)
				i=1	i=2	i=3	i=4	i=5	i=6	i=7	i=8	
S1	L /3	0.2	50.74	18.13	30.07	8.45	9.11	4.36	2.36	2.78	24.73	6.84
S2	L /3	0.4	49.39	37.05	25.63	7.01	5.87	2.88	1.52	1.42	18.63	9.44
S3	L /3	0.6	48.5	46.78	22.58	6.08	4.52	2.23	0.85	1.01	15.96	10.73
S4	L/2	0.2	51.82	10.11	30.91	8.7	10.50	4.92	2.61	3.88	28.37	5.64
S5	L/2	0.4	50.59	24.55	28.74	8.14	7.23	3.87	2.02	1.92	23.52	7.72
S6	L/2	0.6	49.6	39.98	23.93	6.85	5.83	2.68	1.41	1.37	17.94	9.83
S7	2L/3	0.2	49.75	0	34.37	9.85	11.86	5.63	3.02	4.52	30.75	4.33
S8	2L/3	0.4	49.46	20.22	29.98	8.35	7.97	4.14	2.20	2.47	24.67	7.14
S9	2L/3	0.6	48.69	34.71	26.39	7.19	6	3.16	1.56	1.48	19.51	9.13

Specifically, with the reduction of notch length from 0.6 to 0.2 at notch positions of L/3, L/2, and 2L/3 relative to the incident bar, the weight percentage of particles in the largest size group (12–22 mm) decreased from 46.78% to 18.3%, 39.98% to 10.11%, and 34.71% to 0%, respectively. These changes correspond to reductions of 61.24%, 74.71%, and 100% in this size fraction, respectively. Conversely, the weight percentages of particles in the next six size groups, which include the size ranges 12 to 4.76 mm, 4.76 to 4 mm, 4 to 2.38 mm, 2.38 to1.68 mm, 1.68 to1.41 mm, and less than 1 mm, increased significantly with decreasing notch length. This trend indicates an increase in fragmentation intensity and production of finer particles as a result of reduced notch length at various positions.

In general, as the notch length decreases and its distance from the incident bar increases, the average particle size decreases; this trend indicates a gradual increase in the susceptibility and fragmentation intensity of the specimens under dynamic loading. These changes can be approximately classified into three distinct stages.

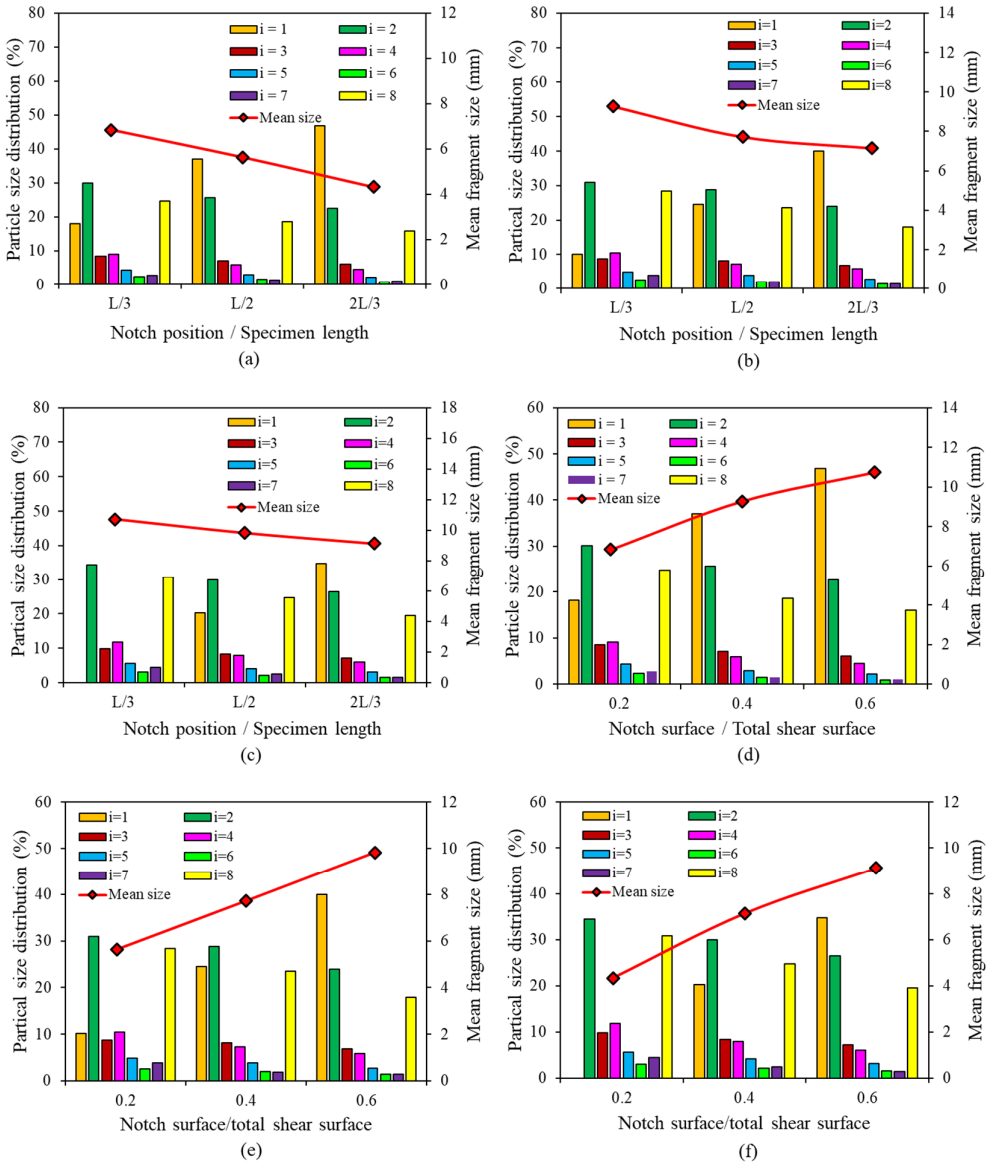

Figure 17. Fragment size distribution and the variation of mean fragment size with respect to notch length and its position relative to the incident bar.

3.7. Fractal dimension properties in fragmented specimens

The fractal dimension serves as an effective quantitative index capable of evaluating the degree of fragmentation of iron ore samples under dynamic loading conditions in SHPB tests. This parameter enables a more precise analysis of the variations in sample damage under different notch geometries, including notch length and its position relative to the incident bar. Investigations indicate a direct relationship between the fractal dimension and the extent of sample damage; in other words, as fragmentation intensity and the damaged area within the sample increase, the calculated fractal dimension value significantly rises. In this study, the fractal dimension is computed based on the mass-equivalent fragment size distribution. The mathematical relationships used for fractal dimension calculation are as follows:

$$D = 3 - d \tag{9}$$

$$d = \frac{Log\,(M_R/M)}{Log\,R} \tag{10}$$

where D represents the fractal dimension of the fragments, d is the slope of the fitted line in the logarithmic coordinate system, M_R denotes the cumulative mass of fragments with diameters smaller than R, and M is the initial mass of the

sample. The linear plots of the logarithmic ratio log (M_R/M) versus log R under different notch lengths and positions relative to the incident bar were constructed based on Equation 10 and were illustrated in Figure 18. The slope of each line, denoted by *d*, was calculated. Subsequently, by substituting the value of *d* into Equation 9, the fractal dimension (*D*) of the fragments resulting from the failure of the iron ore samples was obtained.

Table 2. Cumulative mass and fractal dimension of fragmented iron ore specimens with various notch lengths and positions relative to the incident bar

Specimen No.	Fissure position	notch length	M (g)	Cumulative mass, M_R (g)								Slope (d)	Fractal dimension (D)
				0-1 mm	0-1.41 mm	0-1.68 mm	0-2.38 mm	0-4 mm	0-4.76 mm	0-12.5 mm	0-22 mm		
S1	L /3	0.2	50.74	24.73	27.51	29.88	34.23	43.34	51.79	81.87	100	0.460	2.540
S2	L /3	0.4	49.39	18.63	20.04	21.56	24.44	30.31	37.32	62.95	100	0.613	2.387
S3	L /3	0.6	48.5	15.96	16.97	17.81	20.04	24.56	30.64	53.22	100	0.701	2.299
S4	L/2	0.2	51.82	28.37	32.25	34.85	39.77	50.27	58.97	89.89	100	0.393	2.607
S5	L/2	0.4	50.59	23.52	25.44	27.46	31.33	38.56	46.71	75.45	100	0.502	2.498
S6	L/2	0.6	49.6	17.94	19.31	20.73	23.41	29.23	36.09	60.02	100	0.632	2.368
S7	2L/3	0.2	49.75	30.75	35.28	38.29	43.92	55.78	65.63	100	100	0.346	2.654
S8	2L/3	0.4	49.46	24.67	27.13	29.34	33.48	41.45	49.80	79.78	100	0.471	2.529
S9	2L/3	0.6	48.69	19.51	20.99	22.55	25.71	31.71	38.90	65.29	100	0.591	2.409

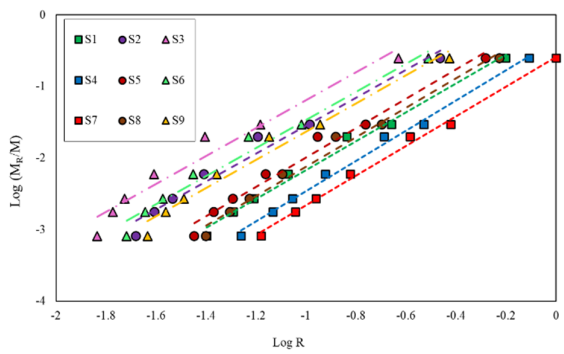

Figure 18. Log (M_R/M) versus Log R curves for different notch lengths and positions relative to the incident bar.

Figure 19 illustrates the variation trend of the fractal dimension of fragmented iron ore specimens based on the notch length and its position relative to the incident bar. According to the results shown in this figure, the fractal dimension *D* increases logarithmically with decreasing notch length and increasing distance from the incident bar. For example, as the notch length decreases from 0.6 to 0.2, the fractal dimension values at notch positions of L/3, L/2, and 2L/3 relative to the incident bar increase from 2.299 to 2.540, 2.368 to 2.607, and 2.409 to 2.654, respectively. Given that the fractal dimension is directly related to the degree of fragmentation, it can be inferred that reducing the notch length and increasing its distance from the incident bar result in a gradual increase in the fragmentation intensity of the specimens. This trend indicates that more effective transmission of impact energy to the regions beneath the notch activates broader failure mechanisms, intensifies the crushing process, and increases the production of fine particles within the sample structure.

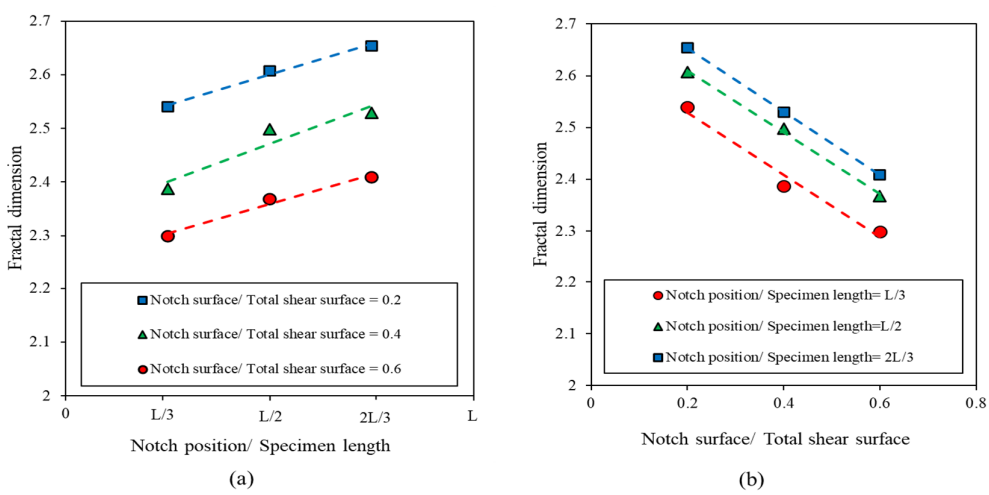

Figure 19. Fractal dimension of specimens and fitted curves affected by notch length and position relative to the incident bar: (a) different notch positions; (b) different notch lengths.

3.8. One-way ANOVA and sensitivity analysis

In this section, the statistical significance and relative influence of notch position and notch length on the investigated mechanical and microstructural parameters, namely dynamic compressive strength, reflected energy (UR), transmitted energy (UT), dissipated energy (UD), mean fragment size, and fractal dimension, were quantitatively evaluated using one-way analysis of variance (ANOVA). For each parameter, ANOVA was conducted separately for notch position and notch length, and the effect size was quantified using Eta Squared (η^2), representing the proportion of the total variance explained by each factor and serving as a sensitivity index.

The results (Table 3) show that notch position exhibited moderate effect sizes ($\eta^2 \approx 0.17–0.22$), indicating that it accounts for roughly 17–22% of the total variance in the studied responses. Although the corresponding p-values (0.467–0.562) are above the conventional 0.05 threshold, meaning the differences among positions are not statistically significant at the 95% confidence level, its effect size values suggest a non-negligible contribution that could become statistically significant in a larger sample set or under different experimental conditions. In comparison, notch length demonstrated consistently strong statistical significance across all responses, with p-values between 0.008 and 0.013 and large effect sizes ($\eta^2 \approx 0.76–0.80$), explaining the majority of variance in mechanical and microstructural properties. This confirms that notch length is the most influential geometric factor within the tested parameter space.

Overall, the sensitivity analysis indicates that while notch length plays the dominant role in governing both strength-related and fracture-surface parameters, notch position also contributes meaningfully to the observed variability and should not be entirely disregarded in design considerations.

Table 3. Results of one-way ANOVA and sensitivity analysis (η^2) for the effects of Notch Length and Notch Position on mechanical and microstructural parameters.

Response	Notch position			Notch length		
	F-statistic	P-value	η^2	F- statistic	P-value	η^2
Dynamic Compressive Strength	0.7566	0.5093	0.2014	11.443	0.0089	0.7923
reflected energy (UR)	0.7822	0.4990	0.2068	11.328	0.0092	0.7906
transmitted energy (UT)	0.6351	0.5621	0.1748	11.888	0.0082	0.7985
dissipated energy (UD)	0.8678	0.4666	0.2243	9.798	0.0128	0.7656
Mean fragment size	0.7358	0.5178	0.1969	11.462	0.0089	0.7925
Fractal dimension	0.7886	0.4965	0.2081	11.016	0.0098	0.7859

3.9. Properties of fragmentation distribution caused by blasting in open-pit mines

To better align laboratory results with actual blasting processes in open-pit iron ore deposits, the fragment size distribution of damaged iron ore specimens exposed to impact loading under controlled laboratory conditions has been more precisely classified. Following blasting operations in iron ore deposits, large rock fragments often require secondary crushing, which significantly increases operational costs. Conversely, the generation of excessively fine particles contributes to increased dust pollution, flyrock hazards, and safety concerns within the mining environment. These conditions also intensify vibrations and shock waves throughout the site, thereby substantially elevating expenses associated with dust control systems, equipment maintenance, and environmental protection.

Accordingly, minimizing the proportion of both excessively large and excessively fine fragments generated during blasting plays a critical role in effectively controlling extraction costs. In this context, to enable a more accurate analysis of impact-induced damage, the size distribution of fragments produced by blasting was examined in a more detailed and segmented manner. The influence of notch length and its distance from the incident bar was evaluated based on the weight percentages of fragments across various size ranges.

Based on the fragmentation distribution characteristics of iron ore specimens subjected to impact loading and considering the necessity of improving blasting operations in open-pit iron ore deposits, the resulting fragments were categorized into three main groups according to fragment size: large, medium, and fine fragments. The fragment size ranges corresponding to each of these three groups are defined as follows:

1. Large-diameter fragments: This category includes particles with diameters of $d \geq 12.5$ mm and represents the majority of large iron ore blocks that typically require secondary breakage after the initial blasting in iron ore deposits. For instance, in the Galali iron ore mine, the

diameter of such fragments is commonly reported to reach $d \geq 600$ mm.

2. Medium-diameter fragments: This category comprises particles with diameters in the range of 1 mm < d < 12.5 mm, corresponding to the second to the sixth size classes. These fragments are of intermediate scale and generally align with the particle sizes typically produced by blasting operations in iron ore deposits. Normally, fragments within this size range do not require secondary breakage. In the Galali iron ore mine, the size range for fragments falling into this category is reported to be 6 mm < d < 600 mm.

3. Fine fragments: This group consists of particles with diameters of $d \leq 1$ mm, classified as the seventh size group. It includes extremely fine particles, which typically represent a small proportion of the total iron ore generated by blasting and may even appear in the form of fine powder. Economically, these fragments have very low value, and the ultrafine particles are often referred to as mineral dust or fines produced by blasting. Such fines can lead to environmental concerns. In the Galali open-pit iron ore mine, particles with diameters of $d \leq 6$ mm are reported within this category.

Based on the aforementioned method, the distribution characteristics of iron ore fragments across different size ranges were determined by considering both the notch length and its position relative to the incident bar. The results of this analysis are presented in Table 4. Furthermore, Figure 20 shows the change in the mass percentages of the three iron ore fragment groups as a function of notch length and its position relative to the incident bar.

As illustrated in Figure 20, a significant decrease in the mass percentage of large-diameter iron ore fragments is observed with decreasing notch length and increasing its distance from the incident bar. This trend highlights the simultaneous influence of notch geometry on the degree of fragmentation under dynamic loading. For instance, when the notch length is fixed at 0.2 of the specimen lengths, increasing the notch distance from L/3 to L/2 and ultimately to 2L/3 results in a continuous reduction in the mass percentage of large-diameter fragments from 18.3% to 10.11%, and finally to 0%. This decrease occurs linearly, with steep percentage point drops of 44.24% and 100%, respectively. When the notch length is held constant at 0.4 of the specimen lengths, increasing the notch distance from L/3 to L/2 and ultimately to 2L/3 results in a decrease in the mass percentage of large-diameter fragments from 37.05% to 24.55%, and finally to 20.22%. This reduction occurs with a more moderate slope, corresponding to decreases of 33.74% and 17.64%, respectively. Finally, when the notch length is held constant at 0.6 of the specimen lengths, increasing the notch distance from L/3 to L/2 and then to 2L/3 results in a reduction in the mass percentage of large-diameter fragments from 46.78% to 39.98%, and subsequently to 34.71%. In this case, the percentage point reductions are 14.54% and 13.18%, respectively, indicating a more gradual decline compared to the previous cases. These results indicate that in specimens with shorter notches, the effect of increasing the notch distance from the incident bar on the reduction of large-diameter fragments is more pronounced. However, as the notch length increases, the sensitivity of this parameter gradually diminishes.

Overall, with a reduction in notch length from 0.6 to 0.4 and subsequently to 0.2, while maintaining the notch position at L/3 of the specimen length relative to the incident bar, the mass percentage of large-diameter fragments decreases linearly. The corresponding reductions are 22.46% and 51.1%, respectively. Subsequently, when the notch is positioned at L/2 of the specimen length relative to the incident bar, a reduction in notch length from 0.6 to 0.4 and then to 0.2 results in a significantly greater decrease in the mass percentage of large-diameter fragments. The corresponding reductions are 38.59% and 58.82%, respectively. Finally, when the notch is located at 2L/3 of the specimen length relative to the incident bar, reducing the notch length from 0.6 to 0.4 and then to 0.2 results in a substantial reduction in the mass percentage of large-diameter fragments, with reductions of 41.75% and 100%, respectively. These results indicate that as the distance of the notch from the loading source increases, the effect of reducing the notch length on the degree of sample fragmentation is significantly amplified, consequently leading to a substantial increase in the rate of decrease in the percentage of large-diameter fragments.

Analysis of the dynamic test results reveals that decreasing the notch length while increasing its distance from the incident bar results in a significant increase in the mass percentage of medium-diameter fragments. When the notch distance from the incident bar is equal to the one-third of the specimen length (L/3), reducing the notch length from 0.6 to 0.4 and then to 0.2 results in a linear and significant increase in the mass percentage of medium-diameter fragments from 37.26% to 44.32% and finally to 57.13%. This

increase corresponds to relative growth rates of 18.95% and 28.9%, respectively. When the notch distance from the incident bar is equal to L/2 of the specimen length, reducing the notch length from 0.6 to 0.4 and then to 0.2 results in an increase in the mass percentage of medium-diameter fragments from 42.08% to 51.93% and subsequently to 61.52%. This increase occurs with a gentler slope, corresponding to relative growth rates of 23.41% and 18.46%, respectively. Finally, when the notch distance from the incident bar is equal to 2L/3 of the specimen length, reducing the notch length from 0.6 to 0.4 and then to 0.2 results in a rapid and nearly linear increase in the mass percentage of medium-diameter fragments from 45.78% to 55.12% and ultimately to 69.25%. In this case, the relative increases are 20.4% and 25.63%, respectively. Overall, the results indicate that reducing the notch length, particularly at greater distances from the loading source, effectively enhances the production of medium-diameter fragments. The intensity of this increase is dependent on the spatial position of the notch within the specimen and can serve as a valuable indicator for evaluating fracture behavior and comminution characteristics under dynamic loading conditions. The data analysis results indicate that, under conditions of a constant notch length, increasing the notch distance from the incident bar leads to a significant rise in the mass percentage of medium-diameter fragments. However, the magnitude and pattern of this increase depend on the length of the pre-existing discontinuous edge notch, exhibiting distinct behaviors in each case.

When the notch length is held constant at 0.2, increasing the notch distance from L/3 to L/2 and ultimately to 2L/3 of the specimen length results in an increase in the mass percentage of medium-diameter fragments from 57.13% to 61.52% and then to 69.25%. This increasing trend is approximately linear with a steep slope, corresponding to relative growth rates of 7.68% and 12.66%, respectively. For a constant notch length of 0.4, increasing the notch distance from L/3 to L/2 and finally to 2L/3 of the specimen length results in an increase in the mass percentage of medium-diameter fragments from 44.32% to 51.93%, and then to 55.12%. In this case, the increasing trend exhibits a gentler slope, with relative growth rates of 17.17% and 6.14%, respectively. Finally, when the notch length is fixed at 0.6, increasing the notch distance from L/3 to L/2 and ultimately to 2L/3 of the specimen length results in an increase in the mass percentage of medium-diameter fragments from 37.26% to 42.08%, and then to 45.78%. The rate of increase in this case is slower, with relative growth rates of 12.94% and 8.8%, respectively. Overall, these results demonstrate that increasing the notch distance from the loading source, even under constant notch length conditions, has a direct impact on the enhanced production of medium-diameter fragments. However, the intensity and rate of this increase are dependent on the notch length, with shorter notches exhibiting greater sensitivity to changes in notch position and a more accelerated increase in medium fragment generation. This behavior can be considered an indicative parameter for assessing damage propagation mechanisms and fracture development under dynamic loading conditions.

The analysis results indicate that the mass percentage of fine fragments generally increases linearly and significantly with decreasing notch length and increasing distance from the loading source. The intensity and slope of this increasing trend vary depending on the length of the pre-existing notch. For instance, under conditions where the notch length is fixed at 0.2, increasing the notch distance from L/3 to L/2, and finally to 2L/3 of the specimen length results in an increase in the mass percentage of fine fragments from 24.73% to 28.37%, and subsequently to 30.75%. This increase is relatively linear and steep, with relative growth rates of 14.72% and 8.39%, respectively. For a fixed notch length of 0.4, increasing the notch distance from L/3 to L/2, and finally to 2L/3 of the specimen length results in an increase in the mass percentage of fine fragments from 18.63% to 23.52%, and subsequently to 24.67%. This increasing trend exhibits a more gradual slope, with relative growth rates of 26.25% and 4.89%, respectively. When the notch length is fixed at 0.6, increasing the notch distance from L/3 to L/2, and finally to 2L/3 of the specimen length results in an increase in the mass percentage of fine fragments from 15.96% to 17.94%, and ultimately to 19.51%. In this case, the rate of increase is slower, with relative growth rates of 12.4% and 8.75%, respectively.

Generally, the results indicate that increasing the notch distance from the loading source, while keeping the notch length constant, leads to an enhanced production of fine fragments. This effect is more pronounced for shorter notches, suggesting that a reduction in notch length increases the specimen's sensitivity to notch position displacement, thereby promoting greater fine particle generation during the fracture process.

This finding can contribute to a better understanding of the comminution mechanisms under dynamic loading conditions. The results of the investigations demonstrate that a reduction in notch length, particularly at different positions relative to the loading source, results in a remarkable increase in the mass percentage of fine fragments. The magnitude and trend of this increase are dependent on the notch position along the specimen length.

When the notch distance from the incident bar is fixed at L/3 of the specimen length, reducing the notch length from 0.6 to 0.4 and then to 0.2 results in a significant and linear increase in the mass percentage of fine fragments from 15.96% to 18.63%, and subsequently to 24.73%. These increases correspond to relative growth rates of 16.73% and 32.74%, respectively, highlighting the significant role of notch length reduction in enhancing fine particle production at this position. When the notch distance from the incident bar is equal to half the specimen length (L/2), reducing the notch length from 0.6 to 0.4 and then to 0.2 results in an increase in the mass percentage of fine fragments from 17.94% to 23.52%, and subsequently to 28.37%. In this case, the increasing trend exhibits a more gradual slope, with relative growth rates of 31.1% and 20.62%, respectively. Finally, when the notch distance from the incident bar equals two-thirds of the specimen length (2L/3), reducing the notch length from 0.6 to 0.4, and then to 0.2, causes a rapid and nearly linear increase in the mass percentage of fine fragments from 19.51% to 24.67%, and then to 30.75%. In this case, the relative growth rates are 26.45% and 24.65%, respectively. These findings clearly demonstrate that reducing the notch length, especially at larger distances from the loading source, significantly increases the production of fine fragments. Therefore, in designing fracture geometry under dynamic loading conditions, careful consideration of both notch length and position can play a crucial role in controlling the size distribution of resulting fracture fragments.

Table 4. Characteristics of iron ore block size distribution based on notch length and Its position relative to the incident bar

Fragment scale	percentage of iron ore fragments m_{iv} under the influence of notch length and its distance from the incident bar.								
	S1	S2	S3	S4	S5	S6	S7	S8	**S9**
Large	18.13	37.05	46.78	10.11	24.55	39.98	0	20.22	**34.71**
Medium	57.13	44.32	37.26	61.52	51.93	42.08	69.25	55.12	**45.78**
Powder	24.73	18.63	15.96	28.37	23.52	17.94	30.75	24.67	**19.51**

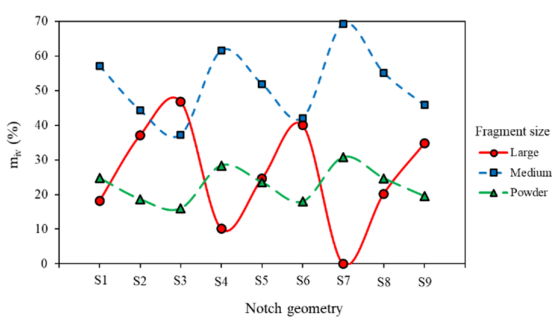

Figure 20. The mass percentage variations of three distinct groups of iron ore fragments under different notch lengths and positions relative to the incident bar.

3.10. Implications for Field-Scale Blast Design

Although the results presented in this study were obtained under controlled laboratory conditions, they provide valuable insights for improving blast design and execution in open-pit iron ore mining. The non-persistent edge notches investigated here can be regarded as analogues to natural discontinuities present within rock masses, which are inherently uncontrollable during blasting. The laboratory findings show that increasing notch length or positioning the notch closer to the loading source (incident bar) leads to reduced dynamic strength, earlier energy dissipation, and the formation of coarser fragmentation, whereas shorter notches located farther from the loading source preserve higher strength and promote more controlled fracture patterns. These observations can inform practical decisions in field-scale operations. For instance, understanding the effect of notch length and position on fragment size distribution can guide the selection of blast hole orientation, explosive charge length, and precise delay timing to achieve desired fracture patterns, minimize flyrock, and prevent unintended rock breakage. Future studies should focus on translating these laboratory findings into actionable guidelines for blast hole design, charge configuration, and delay timing while considering actual field parameters and the heterogeneous nature of rock masses. Such efforts would help bridge the gap between controlled experiments and complex field operations, ultimately enhancing the

efficiency and cost-effectiveness of large-scale blasting processes.

4. Limitation of the present study

The experimental test in this study was conducted exclusively on rock specimens collected and prepared from the Galali iron ore open-pit mine. While this approach ensured consistency in lithology and structural characteristics, it inherently constrains the generalizability of the results to other geological settings. Variations in lithological composition, joint orientation and spacing, weathering degree, and in-situ stress conditions across different sites can significantly alter rock failure modes, fracture propagation patterns, and energy dissipation mechanisms during blasting. Furthermore, site-specific factors, such as blasting history, scale effects, and local stress redistribution, may introduce additional variability that was not captured within the scope of this investigation. Therefore, caution should be exercised when extrapolating the present findings to geological environments with substantially different geomechanical conditions, and the interpretations presented here should be considered representative primarily of settings similar to the Galali mine.

5. Conclusions

Drawing upon the analyses presented, one may infer that reducing the notch length and increasing its distance from the incident bar effectively decreases the mass percentage of large-diameter fragments. Consequently, the amount of iron ore requiring secondary crushing is reduced, leading to controlled costs associated with secondary crushing operations. However, these changes cause a progressive increase in the mass percentage of fine fragments. This increase significantly raises the costs associated with dust control, flyrock, and air blast phenomena in iron ore mines. In light of these two aspects, two key criteria are proposed for evaluating the effectiveness of blasting operations:

1. For a notch length of 0.2 at various notch positions relative to the incident bar, and for a notch length of 0.4 at positions of L/2 and 2L/3 of the specimen length from the incident bar, the mass percentage of medium-diameter fragments exceeds 50%. As a result, over half of the blasted iron ore consists of medium-sized fragments suitable for direct transfer to the next stage of ore processing, thereby eliminating the need for additional crushing.
2. The mass percentage of fine fragments is less than 20% for a notch length of 0.6 at various notch positions relative to the incident bar, and for a notch length of 0.4 at a distance of one-third of the specimen length from the incident bar. Considering the costs associated with iron ore extraction in open-pit mines, the expenses related to dust control (including both economic and temporal costs) are substantial. Therefore, the ultimate effectiveness of blasting operations necessitates minimizing dust pollution as much as possible. Accordingly, the mass percentage of fine fragments should be maintained within a reasonable and controlled range.

According to the two guiding principles discussed above, blasting effectiveness can be assessed by examining how fragment size distribution changes with notch length and distance from the incident bar, as summarized in the following observations:

1. The mass percentage of medium-diameter fragments is less than 50% for a notch length of 0.4 at a notch distance of L/3 of the specimen length from the incident bar, and for a notch length of 0.6 at L/3, L/2, and 2L/3 of the specimen length. Therefore, the crushing effect induced by impact within this range of notch lengths and positions is considered weak.
2. The mass percentage of Large-diameter fragments is less than 20% for a notch length of 0.2 at L/3, L/2, and 2L/3 of the specimen length from the incident bar. Therefore, the need for secondary crushing within this range of notch lengths and positions is reduced.
3. The mass percentage of fine fragments exceeds 20% for a notch length of 0.4 at notch distances of L/2 and 2L/3 of the specimen length from the incident bar, as well as for a notch length of 0.2 at L/3, L/2, and 2L/3 of the specimen length.

The dynamic compressive strength of the rock increases linearly with decreasing notch length and increasing notch distance from the incident bar. Additionally, the energy dissipated in the iron ore samples was significantly influenced by both the notch length and its distance from the incident bar. The dissipated energy exhibited an inverse relationship with notch length and a positive correlation with notch distance from the incident bar. Moreover, the dissipated energy of the samples demonstrated a quadratic relationship with their dynamic compressive strength, which was nearly independent of the notch length and distance from the incident bar. Except for the specimen featuring a notch surface-to-total shear surface a ratio of 0.2 and a notch positioned at 2L/3 of the specimen

length from the incident bar, which failed along a dominant inclined fracture plane at approximately 120°, all other specimens exhibited a characteristic X-shaped fracture pattern. This recurring pattern suggests a symmetrical stress distribution and crack propagation mechanism under dynamic loading, influenced by the interaction between the incident stress wave and the pre-existing notch geometry.

The fragment size distribution of fragmented pieces under impact loading, considering notch length and position relative to the incident bar, aligns well with the two established principles. This indicates that the crushing effect on the iron ore within this range is satisfactory. At greater notch lengths and shorter distances from the incident bar, the mass percentage of fine fragments decreases, whereas the mass percentage of large-diameter fragments increases. In this condition, the mass percentage of medium-diameter fragments falls below 50%. Conversely, at shorter notch lengths and greater distances from the incident bar, the mass percentage of medium-diameter fragments exceed 50%. Under a constant pressure of 12.5 MPa, decreasing notch length and increasing notch distance from the incident bar, reduce the need for secondary crushing and increase the mass percentage of fine fragments. In contrast, greater notch lengths positioned closer to the incident bar increase the need for secondary crushing and reduce the mass percentage of fine fragments. Ultimately, based on the experimental outcomes and the two evaluated principles, the optimal notch length range in this study, defined by the mass percentage of medium-diameter fragments, lies between $0.2 < L < 0.4$, with the notch distance ranging from L/2 to 2L/3.

References

[1]. Kuznetsov, V. M. (1973). The mean diameter of the fragments formed by blasting rock. *Soviet mining science, 9(2), 144-148.*

[2]. Cunningham, C. (1983). The Kuz-Ram model for prediction of fragmentation from blasting. *In Proc. first int. symp. on rock fragmentation by blasting (pp. 439-453).*

[3]. Azizi, A., & Moomivand, H. (2021). A new approach to represent impact of discontinuity spacing and rock mass description on the median fragment size of blasted rocks using image analysis of rock mass. *Rock Mechanics and Rock Engineering, 54(4), 2013-2038.*

[4]. Moomivand, H., & Vandyousefi, H. (2020). Development of a new empirical fragmentation model using rock mass properties, blasthole parameters, and powder factor. *Arabian Journal of Geosciences, 13(22), 1173.*

[5]. Moomivand, H., & Gheybi, M. (2024). Novel empirical models to assess rock fragment size by drilling and blasting. *Measurement, 238, 115375.*

[6]. Moomivand, H., Nayebi, S., Moomivand, H., & Masoumzad, H. (2025). An innovative method to assess specific charge, drilling and blasting costs considering critical factors of rock mass properties, fragment size and blasthole parameters. *Results in Engineering, 106333.*

[7]. Lilly, P. A. (1986). An empirical method of assessing rock mass blastability. *Australia Large Open Pit Mining Conference.*

[8]. Lilly, P. A. (1992, June). The use of the blastability index in the design of blasts for open pit mines. *In Proceedings of Western Australian conference on mining geomechanics, Kalgoorlie, West Australia (pp. 8-9).*

[9]. Moomivand, H., Soltanalinejad, S., & Karwansara, A. M. (2025). Assessment of the optimized stemming length considering rock fragmentation and escape of explosive gases using actual large-scale results. *Results in Engineering, 25, 103575.*

[10]. Soltanalinejad, S., & Moomivand, H. (2024). Development of a novel empirical approach to control overbreak, surface quality, and slope angle of benches following blasting. *Canadian Geotechnical Journal, 62, 1-22.*

[11]. Duan, B., Xia, H., & Yang, X. (2018). Impacts of bench blasting vibration on the stability of the surrounding rock masses of roadways. *Tunnelling and Underground Space Technology, 71, 605-622.*

[12]. Wang, J. W. (2013). The applied research of loose blasting technique in managing crushing accident of fully mechanized coal mining face. *Advanced Materials Research, 734, 863-867.*

[13]. Xie, H. P. (2017). Research framework and anticipated results of deep rock mechanics and mining theory. *Advanced Engineering Sciences, 49(2), 1-16.*

[14]. Xie, H. P., Gao, F., Ju, Y., Gao, M. Z., Zhang, R., Gao, Y. N., ... & Xie, L. Z. (2015). Quantitative definition and investigation of deep mining. *J China Coal Soc 40 (1): 1–10.*

[15]. Li, N. N., Li, J. C., Li, H. B., Liu, T. T., & Chai, S. B. (2015). SHPB experiment on influence of contact area of joints on propagation of stress wave. *Journal of Rock Mechanics and Engineering, 34(10), 1994-2000.*

[16]. Li, Y. X., Wang, Y. Y., & Cao, L. T. (2023). Effects of rough jointed rock mass using 3D printing technology on stress wave energy propagation. *Exp. Mech, 38, 267-275.*

[17]. Wang, L. M., Zhao, J., Hua, A. Z., & Song, H. W. (2003). The progress in study of regularity of a stress

wave propagation in the jointed rock mass. *Rock Soil Mech, 2, 602-605.*

[18]. Pyrak-Nolte, L. J. (1996, December). The seismic response of fractures and the interrelations among fracture properties. *In International journal of rock mechanics and mining sciences & geomechanics abstracts (Vol. 33, No. 8, pp. 787-802). Pergamon.*

[19]. Cai, J. G., & Zhao, J. (2000). Effects of multiple parallel fractures on apparent attenuation of stress waves in rock masses. *International Journal of Rock Mechanics and Mining Sciences, 37(4), 661-682.*

[20]. Zhou, Z., Zhang, L., & Hou, H. J. (2020). Study on impact from filling on mechanical properties and energy evolution of jointed rock mass. *Water Resources and Hydropower Engineering, 51, 117-23.*

[21]. Liu, M., & Liu, E. (2017). Dynamic mechanical properties of artificial jointed rock samples subjected to cyclic triaxial loading. *International Journal of Rock Mechanics and Mining Sciences, 98, 54-66.*

[22]. WANG, P. T., HUANG, Z. J., REN, F. H., ZHANG, L., & CAI, M. F. (2020). Research on direct shear behaviour and fracture patterns of 3D-printed complex jointed rock models. *Rock and Soil Mechanics, 41(1), 4.*

[23]. LI, D., LIU, M., HAN, Z., & ZHOU, Z. (2019). Dynamic compressive mechanical properties of bedding sandstone with pre-existing hole. *Journal of China Coal Society, (5).*

[24]. Li, D., Wong, L. N. Y., Liu, G., & Zhang, X. (2012). Influence of water content and anisotropy on the strength and deformability of low porosity meta-sedimentary rocks under triaxial compression. *Engineering Geology, 126, 46-66.*

[25]. Qiu, J., Li, D., Li, X., & Zhou, Z. (2017). Dynamic fracturing behavior of layered rock with different inclination angles in SHPB tests. *Shock and Vibration, 2017(1), 7687802.*

[26]. Indraratna, B., Jayanathan, M., & Brown, E. T. (2008). Shear strength model for over consolidated clay-infilled idealised rock joints. *Géotechnique, 58(1), 55-65.*

[27]. Indraratna, B., Oliveira, D. A., Brown, E. T., & De Assis, A. P. (2010). Effect of soil–infilled joints on the stability of rock wedges formed in a tunnel roof. *International Journal of Rock Mechanics and Mining Sciences, 47(5), 739-751.*

[28]. Walton, G., Alejano, L. R., Arzua, J., & Markley, T. (2018). Crack damage parameters and dilatancy of artificially jointed granite samples under triaxial compression. *Rock Mechanics and Rock Engineering, 51(6), 1637-1656.*

[29]. Wang, I. T. (2015). Numerical simulation and experimental validation of the Mach reflection effect of shock wave underground surface blast. *Journal of Vibroengineering, 17(3), 1413-1423.*

[30]. Wang, S., Flores-Johnson, E. A., & Shen, L. (2017). A technique for the elimination of stress waves overlapping in the split Hopkinson pressure bar. *Experimental Techniques, 41(4), 345-355.*

[31]. Ding, X., Lu, X., Zhou, W., Shi, X., Luan, B., & Li, M. (2019). Blasting Impact Simulation Test and Fragmentation Distribution Characteristics in an Open-Pit Mine. *Shock and Vibration, 2019(1), 4080274.*

[32]. Field, J. E., Walley, T. M., Proud, W. G., Goldrein, H. T., & Siviour, C. R. (2004). Review of experimental techniques for high-rate deformation and shock studies. *International journal of impact engineering, 30(7), 725-775.*

[33]. Dai, R. P., Guo, X. B., Gong, Q. M., Pu, C. J., & Zhang, Z. C. (2011). SHPB test on blasting damage protection of tunnel surrounding rock. *Rock Soil Mech, 32(1), 77-83.*

[34]. Shi, J. J., Guo, X. B., Xiao, Z. X., & Zhang, Z. (2005). Experimental study on ultrasonic velocity and damage properties of rock under dynamic loading. *Min Res Dev, 25(6), 27-29.*

[35]. Guo, H., Guo, L. J., Zhang, D. N., Liu, X., Qi, Y. D., & Gao, Y. (2015). Application of Hopkinson compressive bar experiment in blasting. *Mod. Mining, 31(3), 174-176.*

[36]. Liu, H. Y., Deng, Z. D., Wang, X. S., Zhang, J. H., & Zhang, L. M. (2014). Similar material test study of dynamic failure of jointed rock mass with SHPB. *Rock Soil Mech, 35(3), 659-665.*

[37]. Ju, Y., Li, Y., Xie, H., Song, Z., & Tian, L. (2006). Stress wave propagation and energy dissipation in jointed rocks. *Yanshilixue Yu Gongcheng Xuebao/Chinese Journal of Rock Mechanics and Engineering, 25(12), 2426-2434.*

[38]. Li, Y. X., Liu, J. F., & Qin, L. (2011). Experimental study on rule of energy dissipation of stress wave across rock joint. *J. Exp. Mech, 26, 85-90.*

[39]. Li, Y., Xie, H., Zhu, Z., Feng, H., & Ye, J. (2009). Study on rules of transmission and reflection of stress wave across fractal joint. *Chinese journal of rock mechanics and engineering, 28(1), 120-129.*

[40]. Li, X. L., Wang, J. G., Zhang, Z. Y., & Huang, Y. H. (2016). Experimental study for effects of strain rates and joint angles on dynamic responses of simulated rock materials [J]. *Explosion and Shock Waves, 36(04), 483-490.*

[41]. Yang, Y. A. N. G., Yang, R. S., & Wang, J. G. (2016). Simulation material experiment on dynamic mechanical properties of jointed rock affected by joint thickness. *Journal of China University of Mining & Technology, 45(02), 211-216.*

[42]. Zhang, W., Zhou, G. Q., Zhang, H. B., & Zhang, Y. (2009). Experimental research on the influence of

obliquity on the mechanical characteristics of a fractured rock mass. *J. China Univ. Min. Technol, 38(1), 30-33.*

[43]. Ping, Q.; Wang, S.; Wu, Y.Y.; Sun, S.J.; Shen, K.; Wang, C.; Gao, Q.; Fang, C. (2022). Study on mechanical properties and energy consumption of fissured sandstone with different dip angles under impact load. *Shock and Vibration, 2022(1), 5335357.*

[44] Wang, J., Gao, Q., Lu, H., Liang, S. F., Huang, B., & Yang, Z. (2015). Impact response tests of layered medium with SHPB. *J. Vib. shock, 34(19), 192-197.*

[45]. Wang, J. G., Liang, S. F., Gao, Q. C., Li, X. L., Wang, L. N., & Zhao, Y. (2018). Experimental study of jointed angles impact on energy transfer characteristics of simulated rock material. *Journal of Central South University (Science and Technology), 49(5), 1237-1243.*

[46]. Du, W., Zhang, D., & Yu, B. (2023). Mechanical and fractal characteristics of sandstone with Pre-existing fissures of different lengths under varying impact loads in SHPB tests. *Theoretical and Applied Fracture Mechanics, 125, 103884.*

[47]. Kim, E., & Changani, H. (2016). Effect of water saturation and loading rate on the mechanical properties of Red and Buff Sandstones. *International Journal of Rock Mechanics and Mining Sciences, 88, 23-28.*

[48]. Xin, C. A. I., Yuan, Z. H. A. O., Lu, C. H. E. N., & Xi-bing, L. I. (2016). Strength characteristics of dry and saturated rock at different strain rates. *Transactions of Nonferrous Metals Society of China, 26(7), 1919-1925.*

[49]. Zhu, J., Deng, J., Ma, Y., Pak, R. Y., & Zhang, Z. (2022). Experimental study on the competing effects of strain rate and water weakening on compressive strength of saturated rocks. *Engineering Geology, 310, 106873.*

[50]. Feng, F., Chen, S., Han, Z., Golsanami, N., Liang, P., & Xie, Z. (2023). Influence of moisture content and intermediate principal stress on cracking behavior of sandstone subjected to true triaxial unloading conditions. *Engineering Fracture Mechanics, 284, 109265.*

[51]. Zhao, Y., Li, Q., Zhang, K., Yang, Y., & Gu, X. (2023). Effect of fissure angle on energy evolution and failure characteristics of fractured rock under uniaxial cyclic loading. *Scientific Reports, 13(1), 2678.*

[52]. You, W., Dai, F., Liu, Y., & Yan, Z. (2022). Effect of confining pressure and strain rate on mechanical behaviors and failure characteristics of sandstone containing a pre-existing flaw. *Rock Mechanics and Rock Engineering, 55(4), 2091-2109.*

[53]. Malachi, Q. T., Zhang, Z. X., Aladejare, A. E., Zhang, N., Paasovaara, N., & Arrieta, M. R. (2024). Effect of strain rate on specific fracture energy and micro-fracture surface properties of rock specimen under dynamic uniaxial compression. *Engineering Fracture Mechanics, 295, 109763.*

[54]. Yan, Z., Dai, F., Liu, Y., & Du, H. (2020). Experimental investigations of the dynamic mechanical properties and fracturing behavior of cracked rocks under dynamic loading. *Bulletin of Engineering Geology and the Environment, 79(10), 5535-5552.*

[55]. Yin, T., Lu, J., Guo, W., Wu, Y., & Ma, J. (2024). Dynamic mechanical response and damage constitutive model of end-jointed rock bridge with different water content states under impact load. *Theoretical and Applied Fracture Mechanics, 130, 104255.*

[56]. Zhu, J., Hu, S., & Wang, L. (2009). An analysis of stress uniformity for concrete-like specimens during SHPB tests. *International Journal of Impact Engineering, 36(1), 61-72.*

[57]. Ping, Q., Luo, X., Ma, Q. Y., & Yuan, P. (2015). Broken energy dissipation characteristics of sandstone specimens under impact loads. *Chin. J. Rock Mech. Eng, 34, 4197-4203.*

انجمن مهندسی معدن ایران
نشریه مهندسی معدن و محیط زیست
نشانی نشریه: www.jme.shahroodut.ac.ir
دانشگاه صنعتی شاهرود

تأثیر آرایش درزه نسبت به میله ورودی در بارگذاری دینامیکی بر اندازه قطعات سنگ‌آهن

شادمان محمدی بلبان‌آباد[۱]، مسعود منجزی[۱] و وهاب سرفرازی[۲*]

۱. گروه مهندسی معدن، دانشکده معدن و مواد، دانشگاه تربیت‌مدرس، تهران، ایران
۲. گروه مهندسی معدن، دانشگاه صنعتی همدان، همدان، ایران

اطلاعات مقاله

تاریخ ارسال: ۲۰۲۵/۰۷/۲۶
تاریخ داوری: ۲۰۲۵/۰۸/۱۶
تاریخ پذیرش: ۲۰۲۵/۱۰/۱۰

DOI: 10.22044/jme.2025.16579.3241

کلمات کلیدی

دستگاه تست فشاری هاپکینسون
شکاف نامتد لبه‌ای
توزیع اندازه قطعات
الگوی شکست
مقاومت فشاری دینامیکی

چکیده

ویژگی‌های توزیع اندازه قطعات ناشی از عملیات آتشباری در معادن روباز تأثیر مستقیم بر عملکرد اقتصادی و بهره‌وری شرکت‌های معدنی دارد. در این مطالعه، آزمایش‌های بارگذاری دینامیکی ضربه‌ای با استفاده از دستگاه تست فشاری هاپکینسون (SHPB) تحت فشار ثابت ۱۲.۵ مگاپاسکال به‌منظور بررسی اثر طول شکاف لبه‌ای و موقعیت آن نسبت به میله ورودی بر توزیع اندازه قطعات سنگ‌آهن انجام شد. با تحلیل ویژگی‌های توزیع خردشدگی نمونه‌ها تحت بارگذاری ضربه‌ای کنترل‌شده در مقیاس آزمایشگاهی، این مطالعه بر مکانیزم‌های بنیادی شکست سنگ که مرتبط با فرآیند آتشباری در معادن روباز سنگ‌آهن است تمرکز دارد. در این راستا، قطعات حاصل از شکست به سه دسته دانه‌بندی شامل قطعات درشت، متوسط و ریز دسته‌بندی شدند. بر مبنای این طبقه‌بندی، تغییرات درصد جرمی قطعات بر حسب طول شکاف و موقعیت آن نسبت به میله ورودی مورد بررسی قرار گرفت. در نهایت، در چارچوب تحلیل خردشدگی در مقیاس آزمایشگاهی، محدوده‌ای مؤثر از طول و موقعیت شکاف لبه‌ای نسبت به میله ورودی برای دستیابی به خردشدگی بهینه شناسایی شد. نتایج نشان داد که طول شکاف بین ۰.۲ تا ۰.۴ و موقعیت آن در فاصله $L/2$ تا $2L/3$ از سمت میله ورودی (که در آن L طول نمونه است)، مطلوب‌ترین توزیع اندازه قطعات را ایجاد می‌کند. این یافته‌ها می‌تواند ارتباط میان رفتار شکست در مقیاس آزمایشگاهی و خردشدگی سنگ در مقیاس میدانی را روشن ساخته و به درک جامع‌تری از فرآیندهای شکست در مهندسی معدن کمک نماید.

نویسنده مسئول مکاتبات: vahab.sarfarazi@gmail.com (و. سرفرازی)